Extreme rainfall events in simulations, theory and related large-scale dynamic processes

Dissertation

Zur Erlangung des Doktorgrades der Naturwissenschaften im

Fachbereich Geowissenschaften der Universität Hamburg

vorgelegt von

Huan Zhang

aus Sichuan, China

Hamburg 2014

Als Dissertation angenommen vom

Fachbereich Geowissenschaften der Universität Hamburg

Auf Grund der Gutachten von Prof. Dr. Klaus Fraedrich

und Dr. Xiuhua Zhua

Hamburg, den 19. Dezember 2013

Prof. Dr. Christian Betzler

Leiter des Fachbereichs Geowissenschaften

Abstract

Extreme rainfall events on various time scales causing floods, generating landslides and damaging ecological systems, get raising concerns under detected climate variability. Many studies show that there is an increasing chance of intense rainfall and flooding in future warmer climates. This thesis aims to further develop an understanding of extreme rainfall following two different aspects: firstly rainfall maxima covering a wide range of time scales and space scales are analyzed revisiting Jennings (1950) observationally established scaling law; and secondly, daily-scales extreme rainfall events are related to large-scale dynamic processes with the aim to provide an extreme value downscaling scheme.

First, global climate model (GCM) simulations are compared with observations in terms of resolution dependence and climate change. The analysis shows the following results: (i) the observed scaling law relating rainfall maxima to duration (Jennings 1950) is basically reproduced but exhibits resolution dependence, (ii) the intensity of rainfall extremes is up to one order of magnitude smaller in the model data, (iii) the increase of rainfall maxima on short time scales in the warmer climate simulations (RCP 8.5) vanishes beyond monthly time scales. The Jennings' law may provide guidance for cascade dependent bias correction of rainfall extremes in simulations.

Then, a conceptual stochastic rainfall model which reveals similar scaling behavior is introduced as a first order auto-regressive process AR(1) to represent the lower tropospheric vertical moisture fluxes, whose upward components balance the rainfall while the downward components are truncated and defined as no-rain. Estimates of ERA-40 vertical moisture flux autocorrelations (at grids near the rainfall stations) provide estimates for the truncated AR(1). Subjected to maximum depth-duration analysis, the scaling coefficient, $b \approx 0.5$, is obtained extending for about two orders of magnitude, which is associated with a wide range of vertical moisture flux autocorrelations $0.1 < a < 0.7$.

Finally, to link daily-scale rainfall extremes with large-scale circulations, extreme value statistics (the Point Process PP, model) is employed to identify warm season (MJJAS) daily-scale rainfall extremes over continental China. The Western Pacific Subtropical High (represented by the WPSH-index) is implanted as a covariate of one or more parameters into the PP model. Observations show that WPSH statistically significant influences extreme rainfall in vast regions except south China. The relation between WPSH and extreme rainfall is also analyzed in MPI-ESM simulated present-day and future climates and then compared with the observations. The results suggest the extreme value statistics as a function of WPSH could be used for statistical downscaling of extreme rainfall events statistics over China.

Abstract

Zusammensassung

Extreme Niederschlagsereignisse verschiedener Zeitskalen bekommen eine wachsende Bedeutung, da sie Hochwasser und Erdrutsche verursachen können, und das Ökosystem schädigen. Zahlreiche vorhergehende Studien zeigen eine zunehmende Wahrscheinlichkeit von Starkniederschlagsereignissen und Fluten in Modellsimulationen eines erwärmten Klimas. Diese Arbeit hat das Ziel, das Verständnis von Extremniederschlägen im Hinblick auf zwei verschiedene Punkte zu erweitern:

1) Niederschlagsmaxima umfassen einen grossen Bereich zeitlicher und räumlicher Skalen, die nach Jennings (1950) Beobachtungen einem Skalierungsgesetz folgen und 2) auf regionaler Skala werden tägliche Extremeniederschläge mit dynamische Prozessen in Verbindung gebracht mit dem Ziel, Grundlagen für ein ‚Downscaling' Schema der Statistik von Extremereignissen zu entwickeln.

Zunächst werden Simulationen eines Globalen Zirkulationsmodells (GCM) mit dem beobachtete Skalierungsgesetz unter dem Aspekt der Klimaveränderung und der Modellauflösung verglichen. Dabei ergeben sich folgende Ergebnisse: (i) das Skalierungsgesetz von Niederschlagsmaxima und -dauer kann im wesentlichen reproduziert werden. Jedoch zeigt sich Auflösungsabhängigkeit. (ii) In den Modellsimulationen ist die Stärke der Niederschlagsereignisse um bis zu einer Größenordnung kleiner als in den Beobachtungen. (iii) Die Zunahme von Niederschlagsmaxima auf kurzen zeitlichen Skalen verschwindet im erwärmten Klima (RCP 8.5) ab monatlichen Zeitskalen.

Ein konzeptionelles stochastisches Niederschlagsmodell, welches ein ähnliches Skalierungsverhalten wie die Beobachtungen aufweist, wird als autoregressiver Prozess erster Ordnung, AR(1), eingeführt, um die unteren troposphärischen vertikalen Feuchtefluss wiederzugeben. Dabei balanciert die Aufwärtskomponente des Flusses den Niederschlag, wohingegen die Abwärtskomponente abgeschnitten und als „kein Niederschlag" definiert wird. Schätzungen der Autokorrelationen des vertikalen Feuchteflusses (ERA-40) an Gitterpunkten nahe von Stationsmessungen liefern Schätzungen für den abgeschnitten AR(1) Prozess. Die Analyse der maximalen Niederschlagsmenge und -dauer ergibt einen Skalierungsparameter von b $\approx$ 0.5, für zwei bis drei Größenordnungen. Diese Wertbereich ist von b mit der Autokorrelationen des vertikalen Feuchteflusses verbunden (mit $0.1 < a < 0.7$).

Abschließend wird die Extremwertstatistik (Punktprozessmodell, PP) für Niederschlagsextreme eingeführt mit der Möglichkeit, Kovariable in einen Parameter (oder mehrere) einzuführen. Als Testgebiet dient das chinesische Festland, das in der warmen Jahreszeit (MJJAS) unter dem Einfluss des West-Pazifische Subtropen-Hochs (dargestellt durch den WPSH Index) steht. Beobachtungen zeigen, dass der WPSH

Index statistisch signifikant die extremen Niederschläge in weiten Bereichen (Ausnahme Südchina) beeinflusst. Diese Beziehung zwischen WPSH Index und der Extremwertstatistik der Niederschläge wird für Simulationen (MPI-ESM) des gegenwärtigen Klimas analysiert und mit Beobachtungen verglichen. Das gute Ergebnis ermutigt dieses Verfahrens auch als mögliches ‚Down-Scaling' der Extremwert-Statistik in Abhängigkeit vom WPSH auch (wie hier gezeigt) für Klima-Szenarien einzusetzen.

Content

List of Figures

List of Tables

Chapter 1

Introduction

1.1 Motivation

This June, north Indian state of Uttarakhand suffered devastating floods and landslides caused by a continuous heavy rainfall. This event is the country's worst natural disaster since the 2004 Tsunami, with the estimated death toll of more than 5,700 (Solanki, 2013). Just one month later, most parts of southwest China experienced widespread flooding caused by heavy rainfall, which affected more than six million people in 21 provinces (Zhang, 2013). Among them, Sichuan province was the hardest hit. July 16, Chinese national media "Xinhua" states: "A total of 58 people died and 175 others went missing due to rainstorm-triggered floods and a landslide last week in southwest China's Sichuan Province".

As a major cause for floods, generation of landslides and crop damage etc, extreme rainfall events get raising concerns under detected climate variability (Kunkel et al., 1999; Easterling et al., 2000; Rosenzweig et al., 2002; Schmidhuber and Tubiello., 2007; Wieczorek and Leahy, 2008).

In this chapter, a general introduction provides a brief review of previous and current work on extreme rainfall.

1.2 Definition of extreme rainfall

Extremes can be categorized on the basis of frequency of occurrence (e.g., once per 20 years), intensity (e.g., > 50mm/day defined as storm in China), and the impacts (e.g. economic cost or damage) etc (Beniston and Stephenson, 2004). Each definition on its own has limitations to describe "extremes".

"Extremes" in most analyses of rainfall extremes primarily refer to two types of descriptions relating to the frequency of the occurrence (Klein Tank et al. 2009). One depends on various climate extremes indices, i.e., an event that is as rare as the 10% or 90% quantile of a particular distribution (Tebaldi et al., 2006; Curriero et al., 2001; Zhai et al., 1999, 2005). It normally represents moderately extreme rainfall events with recurrence times of a year or shorter. Since these events occur relatively frequent, changes can be easily detected and results are overall robust. The other one depends on the application of an asymptotic extreme value theory (Katz, 1999), i.e.

employing the Generalized Extreme Value (GEV) distribution to approximate the distribution of annual maximum rainfall. This type is normally linked with extreme events with re-occurrence times of multi-year to multi-decade (e.g., Kharin and Zwiers, 2005; Kharin et al., 2007; Feng et al., 2007).

Extreme value theory (details see, Coles, 2001; Coles and Pericchi, 2003) is widely used for analyzing extreme rainfall events. It mainly comprises two ways, which are similar as the methods mentioned previously, to define an extreme rainfall event: (i) the maximum of a number of data in a given block; (ii) the intensity of an occurrence larger than a specific threshold. For the latter definition, rainfall extremes are considered as independent exceedances of a specific threshold. Extremes are commonly located in the tail of a stable probability density function. Due to the different way to define the extremes, block maxima or peak over threshold (POT), the tail data can be fitted to GEV or the generalized Pareto distribution (GPD). Kharin and Zwiers (2005) fitted the GEV distribution to annual maxima of near-surface temperature and 24-h rainfall amounts to calculate the 20-year return value, using different daily model output in a period of 20-yr which simulated by an ensemble of CGCMs in IPCC AR4. They used the 20-year return value to express climate extremes, compared present-day simulated extremes with observations and analyzed future scenario extremes under climate change. Combining POT method, Li et al. (2005) used a GPD model to interpret a limiting distribution of observed winter rainfall that lie above a given threshold. Using five time series from geographically dispersed weather stations in Southwest Western Australia, they calculated the return periods for two separate periods 1930–1965 and 1966–2001 and found return periods for the winter extreme daily rainfall have increased after 1965.

1.3 Scaling in extreme rainfall events

The description of a general space-time statistical structure of rainfall is a vital issue in meteorology, and the main subject of a wide literature (e.g., Austin and Houze, 1972; Zawadzki, 1973; Lovejoy and Mandelbrot, 1985; Schertzer and Lovejoy, 1987; Crane, 1990). Atmospheric processes for rainfall normally are considered complicated, combining various non-linear processes in different temporal and spatial characteristic scales. Rainfall events whose temporal scales vary from seconds to years (e.g. drought) comprise physical processes from spatial scales of 10^{-5}m (condensation effect) to scale of 10^{6}m (large-scale air mass and moisture transfer). The demand of linking rainfall statistical properties at different scales is more or less satisfied with development of the theory of self-organized-criticality (SOC) and multifractals which generally obey a scale invariance property, namely scaling behavior (Lovejoy and Schertzer, 1985, 1990, 2006; Tessier et al., 1993, 1996; Davis

et al., 1994; Schertzer and Lovejoy, 1987; Verrier et al., 2010). Even though a lot of work has been done to establish the multifractal properties of rainfall temporally and spatially, the terminology, notation and analysis of multifractal processes are not standardized (Vaneziano et al., 2006). Besides, under multifractal framework, scale properties in the rainfall process normally have been investigated without taking into account the rain generation mechanisms. Various methods are used to describe different scaling behavior of rainfall in multi time-scales. Fraedrich and Larnder (1993) applied temporal power spectrum analysis on sets of daily and 5-min rainfall time series in Europe. The ensemble mean power spectra show distinct scaling regimes of rainfall in continental Europe: < 2.4h, $b \approx 1$ (1/f noise); between 2.4 h and 3 days (frontal systems), $b \approx 0.5$; between 3 days and 1 month (general circulation fluctuations), a transition regime; between 1 month and 3 years a spectral plateau with $b \approx 0$; > 3 years (climate variability), $b \approx 0.7$ (the power spectrum exponent, $0 \leqslant b \leqslant 1$; $b = 0$: white noise; $b = 1$: pink noise). Marini (2005) presented the variance of temporal and spatial rainfall to the scale using sets of high resolution observation data (from 2s to 1 hour in time and 4 km in space). He suggests existence of three temporal regimes for time scales between 1s to around 10 days: inner regime (1 min ~ 15 min), transition regime (15 min ~ 80 hours) and scaling regime (> 80 hours); and two spatial regimes for spatial scale between 4 km and 100 km: inner regime (4 km ~ 20 km) and transition regime (> 20 km).

Even before discovery of the Gutenberg-Richter scaling law (Gutenberg and Richter, 1954), which is a relation for earthquake numbers and magnitude, a scaling law relating the global maximum of rainfall to durations has already been discovered by Jennings (1950, shown in figure 1.1).
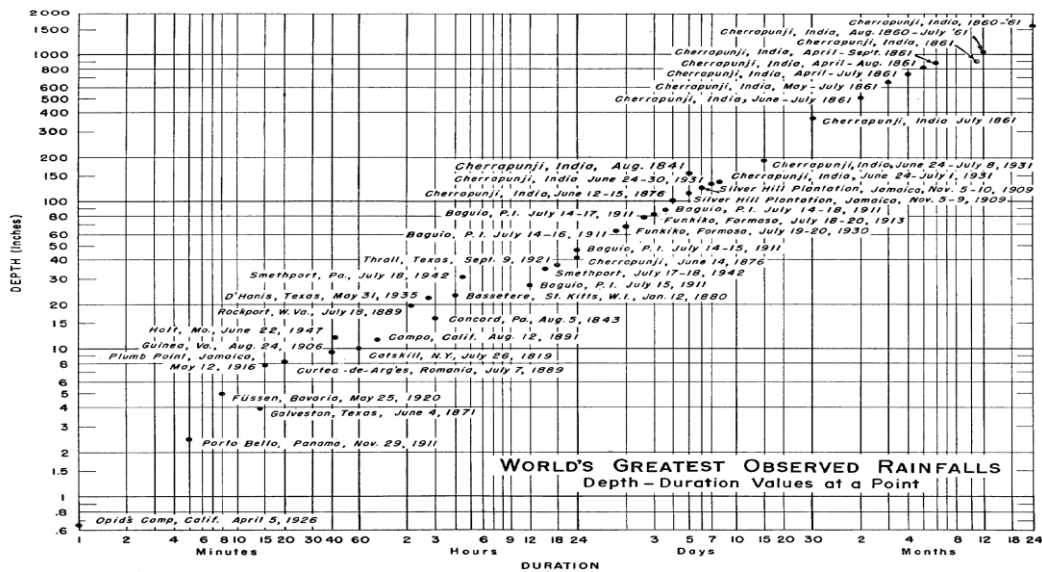
Figure 1.1: The values of the depths and durations of the world's greatest observed point rainfalls (Jennings, 1950).

The startling scaling law relationship can be expressed as $P \sim d^{\,b}$ with $b \approx 0.5$ between the global maximum of rainfall P and durations d. This simple relation is valid in a range from minutes to years, hence on six orders of magnitude. For durations shorter than 3 days, records are from different locations over tropics and subtropics; for longer durations world-wide records mainly include three rain spells from three locations: Cherrapunji (India) and Commerson and Foc Foc (La Reunion). The result of Jennings (1950) entered hydrology textbooks, papers and reports, and has been substantiated since with more stations and extended records becoming available (Paulhus 1965; Eagleson 1970; Hubert et al., 1993; WMO, 1986, 1995; Galmarini et al., 2004). The plot of records later was reproduced by Paulhus (1965) and Galmarini et al. (2004) using updated data. As expected, when more data became available, the estimate of record rainfall got improved comparing to smaller record in older data sets. Using the most recent data (Table 1.1), the scaling phenomenon is re-plotted in Figure 1.2. The best-fit line indicates the startling relationship $P \sim d^{\,b}$ with $b \approx 0.5$.

There were two papers commenting on Jennings scaling law. By employing multi-fractal methodology, Hubert et al. (1993) connected the scaling exponent to a singularity parameter with a multi-fractal analysis, but there is no rainfall mechanism involved. Galmarini et al. (2004) proposed a combination of the rainfall distribution with a time-lag autocorrelation thereby covering scaling ranges of about three decades of duration.

1.4 Rainfall and extreme rainfall under climate change

Although there is no pronouncing evidence of global trends, many studies using observation data show existence of trends in rainfall at continental scales. As addressed in Intergovernmental Panel on Climate Change (IPCC) Fourth Assessment Report (AR4, IPCC, 2007), "very likely rainfall increases in high latitudes and likely decreases in most subtropical land regions, continuing observed recent trends".

However, the frequency of heavy rainfall events is reported to increase over most areas across the globe in the past 50 years. For example, Groisman et al. (2005) used several dataset which covering half of the land area of the globe, and found the very heavy rainfall, defined as the upper 1% of daily rainfall events, to exhibit a widespread increase in the mid-latitudes in the past 50－100 years. Alexander et al. (2006) found extreme rainfall in stations covering the northern hemisphere midlatitudes and part of Australia display a significant increase in 1979－2003 compared to the period of 1901－1950. Min et al. (2011) found that 65% (61%) of the data-covered areas have positive trends for annual maxima of daily (five-day) consecutive over the period from 1951 to 1999.

Table 1.1: World record point rainfall measurements from National Weather Service (2013)

Duration	Amount (mm)	Location	Start date
1 min	31	Unionville, Maryland, USA	4 Jul 1956
3 min	44	Haughton Grove, Jamaica	30 Sep 1925
5 min	63	Porto Bello, Panama	29 Nov 1911
8 min	126	Fussen, Bavaria, Germany	25 May 1920
15 min	198	Plumb Point, Jamaica	12 May 1916
20 min	206	Curtea de Arges, Romania	7 Jul 1889
30 min	280	Sikeshugou, Hebei, China	3 Jul 1974
42 min	305	Holt, Missouri, USA	22 Jun 1947
60 min	401*	Shangdi, Nei Monggol, China	3 Jul 1975
72 min	440	Gaoj, Gansu, China	12 Aug 1985
2 hr	489	Yujiawanzi, Nei Monggol, China	19 Jul 1975
2.5 hr	550	Bainaobao, Hebei, China	25 Jun 1972
2.75 hr	559	D'Hanis, Texas, USA	31 May 1935
3 hr	724*	Smethport, Pennsylvania, USA	18 Jul 1942
4.5 hr	782	Smethport, Pennsylvania, USA	18 Jul 1942
6 hr	840*	Muduocaidang, Nei Monggol, China	1 Aug 1977
8 hr	1050*	Muduocaidang, Nei Monggol, China	1 Aug 1977
9 hr	1087	Belouve, La Réunion	28 Feb 1964
10 hr	1400*	Muduocaidang, Nei Monggol, China	1 Aug 1977
18 hr	1589	Foc Foc, La Réunion	7 Jan 1966
18.5 hr	1689	Belouve, La Réunion	28 Feb 1964
20 hr	1697	Foc Foc, La Réunion	7 Jan 1966
22 hr	1780	Foc Foc, La Réunion	7 Jan 1966
1 day	1825	Foc Foc, La Réunion	7 Jan 1966
2 day	2467	Auré re, La Réunion	7 Jan 1958
3 day	3929	Commerson, La Réunion	24 Feb 2007
4 day	4869	Commerson, La Réunion	24 Feb 2007
5 day	4979	Commerson, La Réunion	24 Feb 2007
6 day	5075	Commerson, La Réunion	24 Feb 2007
7 day	5400	Commerson, La Réunion	24 Feb 2007
8 day	5510	Commerson, La Réunion	24 Feb 2007

Table 1.1: continued

Duration	Amount (mm)	Location	Start date
9 day	5512	Commerson, La Réunion	24 Feb 2007
10 day	5678	Commerson, La Réunion	18 Jan 1980
11 day	5949	Commerson, La Réunion	17 Jan 1980
12 day	5949	Commerson, La Réunion	16 Jan 1980
13 day	6072	Commerson, La Réunion	15 Jan 1980
14 day	6082	Commerson, La Réunion	15 Jan 1980
15 day	6083	Commerson, La Réunion	14 Jan 1980
1 month	9300	Cherrapunji, Meghalaya, India	1 Jul 1861
2 month	12767	Cherrapunji, Meghalaya, India	1 Jun 1861
3 month	16369	Cherrapunji, Meghalaya, India	1 May 1861
4 month	18738	Cherrapunji, Meghalaya, India	1 Apr 1861
5 month	20412	Cherrapunji, Meghalaya, India	1 Apr 1861
6 month	22454	Cherrapunji, Meghalaya, India	1 Apr 1861
11 month	22990	Cherrapunji, Meghalaya, India	1 Jan 1861
1 year	26461	Cherrapunji, Meghalaya, India	1 Aug 1860
2 year	40768	Cherrapunji, Meghalaya, India	1 Jan 1860

* indicates estimated value. Coordinates are approximate.
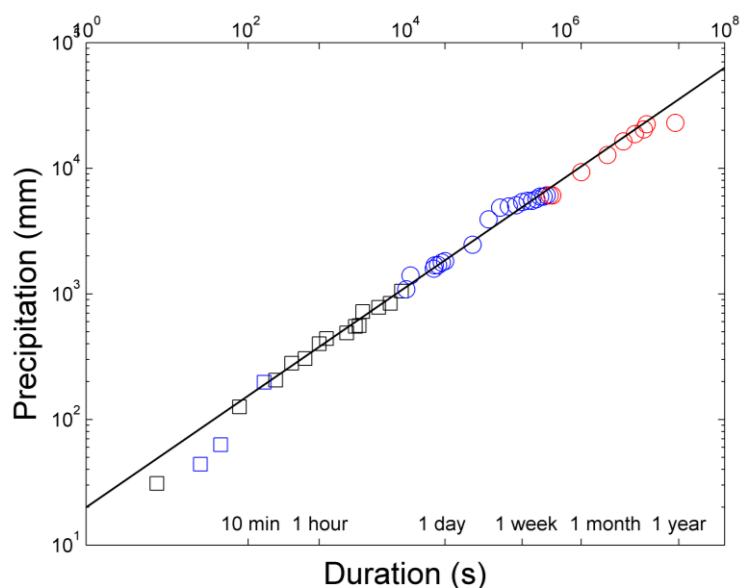
Figure 1.2: Same as figure 1.1, but using the most recent data in table 1.1. Blue markers: records from tropics; blue circles: records from La Réunion; red circles: records from Cherrapunji, India.

The reason is that extreme rainfall is proportional to the availability of water vapor content. However, mean rainfall is associated with surface-energy balance, e.g. when surface receives more long-wave radiation, more rainfall would be generated to release extra energy as latent heat; or the ability of the atmosphere to radiate long-wave energy (Bates et al., 2008; Stephens et al. 2012).

A greater increase is expected in frequency and intensity of extreme events in future warm scenario suggested by IPCC AR4 model simulations and also theoretical studies; and these changes could occur even with relatively small mean climate changes. Consistent with more extreme rainfall events, there is an increased chance of intense rainfall and flooding in future warmer climate. These estimations were later confirmed by a subsequent assessment by the IPCC in its special report on "Managing the Risks of Extreme Events to Advance Climate Change Adaptation" (SREX) (IPCC, 2012). With the growth of population and impact of human activities, environment and society are vulnerable and susceptible to extreme events. Therefore, changes to rainfall extremes associated with climate change are one of the most important issues of concern.

Although global climate models (GCMs) support the claim that rainfall will increase in many regions of the world in future warmer climate, and provide rainfall frequency and intensity projections, fine resolution simulations generated from statistical or dynamical approaches are still required to assess changes in rainfall extremes (e.g. Jones et al., 2009). Most models can quite well simulate light to middle rainfall, but has poor ability to simulate heavy rainfall events (Durman et al. 2001; Alexander and Arblaster, 2009). Kharin et al. (2013) assessing the performance of the Coupled Model Intercomparison Project (CMIP5) models, found the models to overall agree with the observations in 20-year return value of extreme rainfall in the extratropics. However, there remain large uncertainties in simulated extreme rainfall, especially in tropical and subtropical regions. Relative (%) increases in the intensity of rainfall extremes generally exceed those for annual mean rainfall under global warming. Globally averaged, the CMIP5 multi-model 20-year return value increase is about 6% in the RCP2.6 experiment, 10% in the RCP4.5 experiment and more than 20% in the RCP8.5 experiment by the end of the 21st century.

As extreme events are more uncertain than normal data, more work on the extremes under climate scenarios is necessary.

1.5 Downscaling methods

To fill the gap between the resolution of output from GCMs and required data in finer resolution, downscaling is used as a strategy to provide locally relevant data. There

1 Introduction

are two essentially downscaling methods: dynamic and statistical approaches.

Dynamical downscaling approach provides output at a resolution much higher than a GCM can produce, which is primarily based on the use of regional climate models (RCMs). A RCM is driven by a GCM, and their physical consistency is controlled by the agreement of their large-scale circulations (von Storch et al., 2000). In most cases, RCM-GCMs are one-way coupled, which means RCMs give no feedback to the driving GCMs (IPCC, 2007; Maraun et al., 2010). Technically, the GCMs simulate the response of the global circulation to large-scale forcings, e.g. increasing CO_2 concentrations or increasing radiation forcing. The GCM applies certain driving factors to the RCM, then depending on sub-GCM grid scale forcings the RCM runs similar as a GCM but based on its own physical equations, and output the factors at a fine spatial and/or temporal scale. RCMs at higher spatial resolution provide a better description of the regional topography and/or land cover inhomogeneity. Expectedly, the output variables respecting with orographic effects can be improved (Giorgi and Mearns, 1999). When the resolution is high enough, realistic mesoscale circulations appear (e.g. Murphy, 2000).

Many studies have shown the ability of RCMs to produce more realistic climate comparing to their driving GCMs at regional scales. Bell et al. (2004) coupled National Center for Atmospheric Research Community Climate Model version 3.6.6 (with a horizontal resolution of 2.8° × 2.8°) and the second generation NCAR Regional Climate Model (with a horizontal resolution of 40 km) to construct frequency and intensity of extreme events, including minimum temperature, maximum temperature and extreme rainfall at high temporal and spatial resolution in future climate scenarios for California.

However, RCMs are not expected to certainly improve regional rainfall extremes. Many studies (Rauscher et al., 2009) have shown that the skill of RCMs severely depends not only on the model resolution but also on the region and the season. The primary problem is that significant biases of the simulated mean rainfall on large scales in the driving GCM can be inherited by RCMs (Durman et al., 2001). How to measure system errors in GCMs; and be cancelled is then another acute problem (Christensen et al., 2008). Besides, RCMs commonly suffer from other obvious problems: imperfect parameterization schemes, numerical stability etc (e.g. Lenderink and van Meijgaard, 2008; Maraun et al., 2010; Bachner et al., 2008; Murphy et al., 2009). The output field variable presenting areal-average value, is inconsistency with site-specific data (Chen and Knuston, 2008). Detailed reviews are given by Foley (2010), Rummukainen (2010), and Feser et al. (2011).

An alternative approach of dynamic downscaling is statistical downscaling. Compared to using RCMs at a very high cost of computation sources, statistical downscaling is computationally efficient and inexpensive. Statistical downscaling approaches are divided by Maraun et al (2010) into prefect prognosis, model output

statistics (MOS) and weather generators. Perfect prognosis refers to statistical downscaling relationships being established by observations. For MOS, both RCM simulated data and observations are used to develop downscaling relationship. Weather generators are hybrid downscaling methods by using observations, RCMs simulation data or both. However, studies applying those methods mainly focused on mean, variance and quantiles of rainfall intensity or parameters of the rainfall distribution. Only few studies (Sillmann et al., 2011; Wang and Zhang, 2008) based on extreme value theory validate extreme rainfall intensities (e.g., 20, 50 or 100 year return levels).

Notice that the validity of statistical downscaling is based on an assumption that the empirical relationship identified for the present-day climate will hold for future climate scenarios (Wilby et al., 2004).

1.6 Scope of this thesis

Based on these previous works, the thesis targets to answer a few questions as follows:

➢ Can GCMs simulations with different resolutions (T63 and T31) reproduce Jennings scaling law, the observed maximum rainfall-duration scaling-law relationship? Can Jennings scaling law be found in single grid-points? What kind of information is embedded in the scaling exponent? Do extremes in a warmer climate increase simultaneously on all different time scales compared to the present-day climate?

➢ Can we construct a simple model to simulate Jennings' scaling law? What is the mechanism explanation?

➢ How to relate daily-scale extreme rainfall events with large-scale circulation to understand the dynamics of generation of extremes?

The thesis is mainly composed of three chapters to answer these three questions respectively, besides the first one for the general introduction and last one for summary and discussion. Content from the three chapters are prepared for publication, one is already published, one is accepted and the last one is in preparation. Chapter 2 and Chapter 3 focused on the characteristics of "scale-invariance" Jennings scaling law and the dynamics behind it; and this implies that there will be a partial overlap of some contents between the two chapters. Chapter 4 gives a case study on linking extr-

emes with a large-scale circulation factor, which could be useful as a statistical approach downscaling extremes.

In Chapter 2 and 3, the notion "extreme" will be used for global maximum rainfall events. In Chapter 4, "extreme" means intensity of a rainfall event higher than a threshold, see the text for details.

Chapter 2

Scaling of rainfall extremes versus duration

Section Summary

Rainfall maxima in global climate model (GCM) simulations are compared with observations in terms of resolution dependence and climate change. The analysis shows the following results: (i) the observed scaling law relating rainfall maxima to duration (Jennings 1950) is basically reproduced but exhibits resolution dependence, (ii) the intensity of rainfall extremes is up to one order of magnitude smaller in the model data, (iii) the increase of rainfall maxima on short time scales in the warmer climate simulations (RCP 8.5) vanishes for monthly time scales, (iv) Jennings scaling exponent is found associated with Hurst exponent.

2.1 Introduction

So far, there is no analysis of global climate model (GCM) simulations verifying the observed maximum rainfall depth-duration scaling. One aim of the analysis is to assess the ability of global climate models to represent this behavior on daily to annual time scales. Simulations of two climate models contributing to CMIP5 present-day and global warming experiments (RCP8.5) are used.

It is notable that, Cherrapunji, which is located at 91°42'E, 25°18'N and on the windward flank of the Khasi Hills, holds the world rainfall records from 15 days to two years (Jennings, 1950; Paulhus,1965; Dahr and Farooqui, 1973), and records between 1 day to 15 days are so close to world ones. And those rainfall records from this single station for duration from one day to two years can be fit as a straight line in log-log plot, and its slope is close to 0.5 (Dahr and Farooqui, 1973). And based on the analysis on 11 single stations, including Commerson (La Réunion) which contributes a sequence in world records, Galmarini et al. (2004) shows that single-exponent scaling laws exist for single stations experiencing extremely high rainfall.

When trying to find autocorrelation in observation and simulation data, a close relation is found, between the scaling exponent and Hurst exponent; and this result probably can also be used to understand the existence of the scaling exponent.

The simulations considered in this study are briefly described in Section 2.2. A comparison of the extreme events in simulations with observations by revisiting the scaling law is presented in Section 2.3, followed by a brief conclusion.

2.2 Data and Methods

The GCM simulations used in the present analysis are performed by two state-of-the-art coupled ocean-atmosphere general circulation models: ECHAM5 /MPIOM (EH5OM), ECHAM6/MPIOM (EH6OM) and HadGEM2-ES (HadGEM) with a spectral and a grid point global atmosphere, respectively. The models are being developed by the MPI-M (Max Planck Institute for Meteorology) and the Hadley Center participating in the CMIP5 runs. A detailed description of ECHAM5 is given by Roeckner et al. (2006), ECHAM6 by Stevens et al. (2013), and HadGEM by Jones et al. (2011). Table 2.1 summarizes the basic information on horizontal and vertical resolutions, temporal resolutions, and simulation lengths. Present-day climate ECHAM simulations are compared to estimate resolution dependence. For future climate simulations based on the Representative Concentration Pathway we select RCP8.5 with a continuous rise in radiative forcing during the 21st century leading to a value of about 8.5 Wm^{-2} in 2100 because, if Jennings scaling law exists in the simulation of the high emission scenarios we may expect it to hold also for those with

less emission. For comparison, historical simulations for 1860–2005 by the same models are also analyzed.

Table 2.1: Simulations of present-day (with different resolutions) and future climates

Model and resolutions	Experiment	Record Length
Hadley-Atm: N96L38	RCP8.5 (daily sampling)	2006–2100
Hadley-OM: GR1.0L40	Historical (daily sampling)	1860–2005
MPI-ECHAM6: T63L47	RCP8.5 (daily sampling)	2006–2200
MPI-OM: GR1.5L40	Historical (daily sampling)	1850–2005
MPI-ECHAM5: T63L31	Historical (six hourly sampling)	1800–2000
MPI-OM: GR1.5L40	A1B (six hourly sampling)	2001–2200
MPI-ECHAM5: T31L19	Historical (six hourly sampling)	1860–2000
MPI-OM: GR3.0L40	Full forcing (six hourly sampling)	1860–2000

The greatest point rainfall for different durations are extracted in this way: firstly, use a running window to search for the maximum total from time series of all single grid points either located at land or at sea; secondly, change the window length which means time duration and redo it.

The slopes of the line in logarithm figures are calculated by polynomials least-squares fitting.

2.3 Revisiting Jennings scaling law

The simulations are analyzed without bias correction to focus on the models' non-linear scaling behavior of extremes, although climate models are incapable to provide the correct magnitude of global rainfall (see for example, Haerter et al. 2011). Furthermore, recent developments of bias corrections for rainfall (Haerter et al 2011) suggest a cascade of time scales to be considered, ranging from daily via monthly to annual periods, which however could modify the models' intrinsic scaling behavior.

The greatest point rainfall depths for different durations are extracted: firstly by running a duration-window to search for the maximum total rainfall P from all grid point time series at land and at sea separately and secondly, by continuing with different window lengths d to assess the relationship $P = P_0 (d / d_0)^b$. Rainfall P and P_0 are in mm, and duration d and d_0 in hours. The monthly maximum P_0 is used to quantify the deviations of simulated from observed records.

The global observed maximum rainfall-duration relation serves as a reference to compare the simulated data from land and ocean grid points, which range from six hours or one day to one year. The scaling-law relationship $P = P_0(d / d_0)^b$ is addressed

by a log-log comparison with the exponent $b \approx 0.5$ representing the slope while the logarithm of P_0 is given by the intercept (Figure 2.1a). The results of the simulations are displayed in the same manner with slopes obtained by least-square fits (note that the simulated data are shifted to avoid overlaps; the corresponding factors are included in Figure 2.1a). The following results are noted:

Scaling-law relationships simulated: The maximum rainfall-duration scaling-law exponents as $b \approx 0.5$ in the higher resolutions is obtained (EH5OM T63L31, EH6OM and HadGEM) compared to $b \approx 0.7$ for the lower resolution model EH5OM (T31L19). It is obvious that a reduced temporal resolution reduces the duration range to three (two) orders of magnitude given the six hourly (or daily) sampling, compared with the range of six orders in observations which include rainfall events measured in minutes.

Locations and durations of rainfall maxima: In simulations with T63L31 resolution associated with short duration (≤ 5 days) maxima originate from different locations distributed in Russia, northern China and Australia, which are over a wide range of latitudes; while longer durations (> 5 days) comprise only of a few rain spells which occur mostly over Bengladesh and Papua New Guinea (Figure 2.1b). Rainfall maxima over the ocean are distributed over a wide range of locations in the Pacific and the eastern Bay of Bengal. A similar behavior is observed over land (Jennings, 1950; Galmarini et al., 2004): Rainfall maxima with durations shorter than 6 days, are reported from different locations in the tropics and subtropics, while for longer durations world-wide rainfall records consist of three rain spells from tropical locations Cherrapunji (India), Commerson and Foc Foc (La Reunion). In contrast to simulations with T31L19 resolution, land records are scattered over a wide range of both latitudes and longitude (shown in Figure 2.1c). It appears that with increasing resolution the topography induces localized rainfall maxima.

Rainfall-depths: For all time scales, the magnitudes of maxima are much larger at higher spatial and vertical resolutions (T63L31 versus T31L19). Monthly rainfall maxima P_0 range from $P_0 = 940$ mm in EH5OM (T31L19), 1998 mm in EH5OM (T63L31), 2047 mm in EH6OM (historical) and 2210 mm in EH6OM(RCP8.5), to 3044 mm in HadGEM (historical) and 3165 mm in HadGEM (RCP8.5). At all time scales, simulated maxima are distinctly below the observed ones and the largest
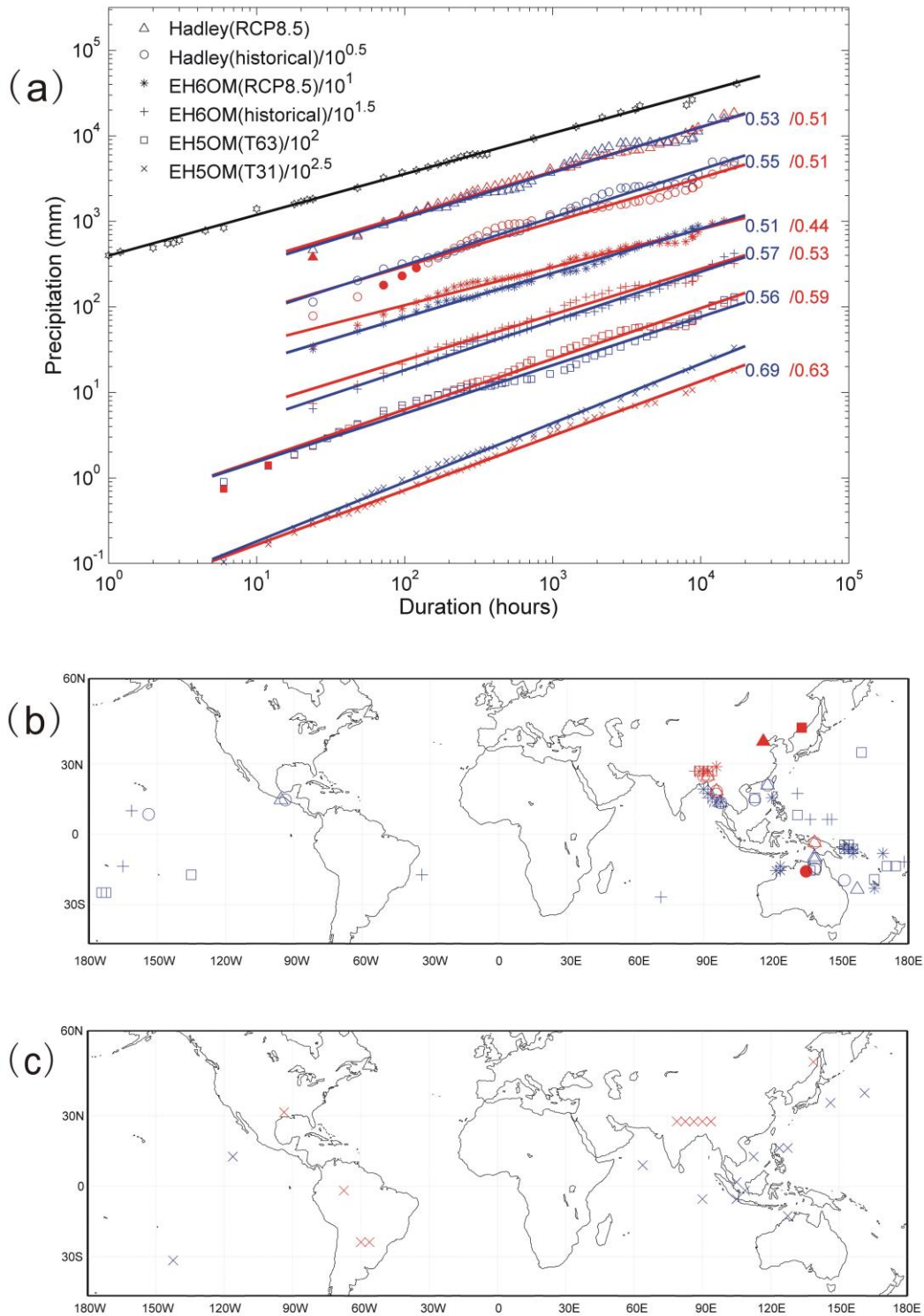
Figure 2.1: (a) Maximum rainfall-duration diagram from observed station data (black) and simulated grid point values over land (red) and ocean (blue). To avoid overlaps simulated records are shifted by the indicated power of 10; thin solid lines indicate fits for land and ocean. (b) Geographical locations of simulated grid point data, symbols are the same as in (a). These values lie far below the observed one month maximum of 10,867 mm.
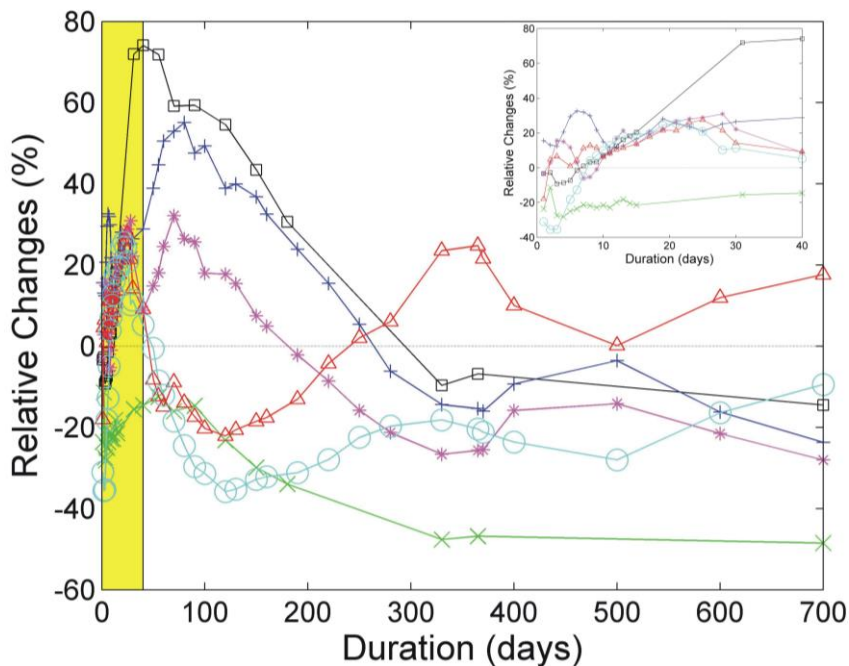
Figure 2.2: Land-ocean comparison: Relative changes of maximum rainfall versus duration between maxima over land compared to ocean in different simulations (symbols as in figure 2.1a): Hadley (RCP8.5, red), Hadley (historical, cyan), EH6OM (RCP8.5, magenta), EH6OM (historical, blue), EH5OM (T63L31, black), EH5OM (T31L19, green).
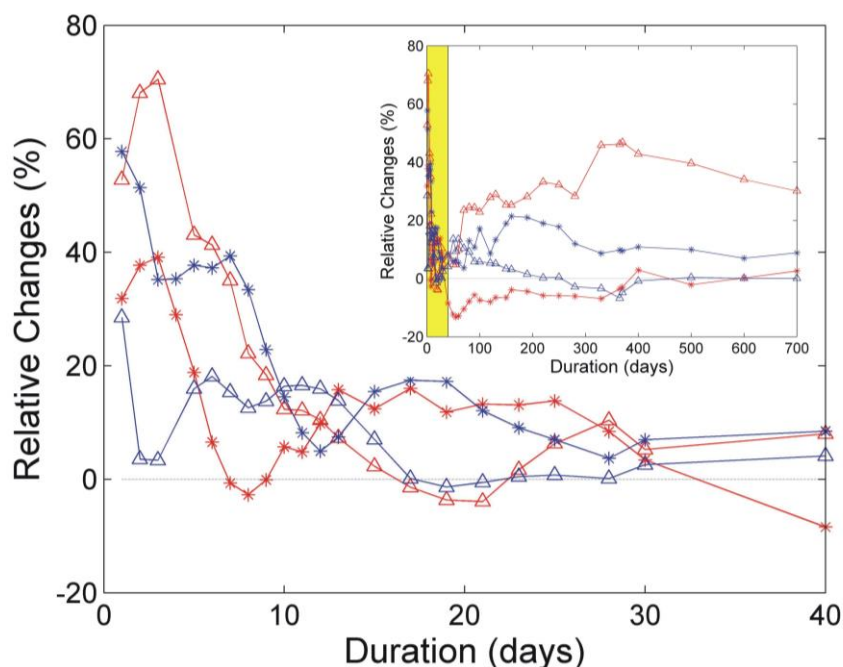
Figure 2.3: Warmer and present-day climates: Relative changes of maximum rainfall versus duration between maxima in warm climate scenarios (RCP8.5) compared to present-day simulations, respectively, over ocean (blue) and land (red) in CMIP5: HadGEM (triangle) and EH6OM (star).

deviation of one order of magnitude is found in the simulations with the lowest resolution of T31L19. This is consistent with findings that the amplitude of extremes increase with resolution in simulations performed with models from the same modeling group (Kharin et al., 2007). Thus, for bias correction of global rainfall extremes from high resolution simulations the observed monthly maximum P_0 needs to be adapted to recover Jennings scaling law. Low resolution models, however, would require a correct cascade related scaling exponent.

Land and ocean: In average, the rainfall maxima over land are higher than ocean in EH5OM (T63T31) for durations below the annual time scale; the opposite holds for EH5OM (T31L19) simulations (Figure 2.2). That is, rainfall maxima are higher over oceans than over continents in low resolution simulations where moisture supply plays the dominant role. With higher resolutions the magnitudes of the rainfall maxima increase in general but the increments are higher over land than over ocean; this may be caused by increased instability due to topographic effects. In a warmer climate, relative changes between the rainfall maxima over land and ocean decrease with longer durations in EH6OM, while they depend on different time scales in HadGEM (Figure 2.2).

Future climates: For warmer climates the higher resolution simulations (RCP8.5, EH6OM and HadGEM) show that rainfall extremes tend to become more severe at shorter time scales over land (Figure 2.3). For durations of days the maximum rainfall depth increased by about 50% while there is almost no change in maximum rainfall for durations of months. Beyond months the models diverge (Figure 2.3, inner panel): HadGEM simulations report rain maxima increasing by 50% at annual time scales, while EH6OM rainfall maxima do not change or decrease up to -10%, compared to their present day simulations. Rainfall extremes over ocean and land show similar behaviour for shorter durations while for long durations HadGEM remains close to zero, and EH6OM increases up to 20%.

Second and third maxima: For all simulations, the second and third rainfall maxima versus duration follow the same scaling law. The differences between the first, second and third maxima are less than 10% at all time scales. That is, the scaling exponent *b* appears to be independent of the rainfall depth. In addition, missing an individual extreme event does not severely change the scaling relationship. Furthermore, extending the analysis to second/third maxima provides a control on outliers affecting the comparison of records, for example in present versus future climates over land and sea. As shown in Figure 2.4, the variations of relative changes calculated from second and third maxima are consistent with those from first maxima.
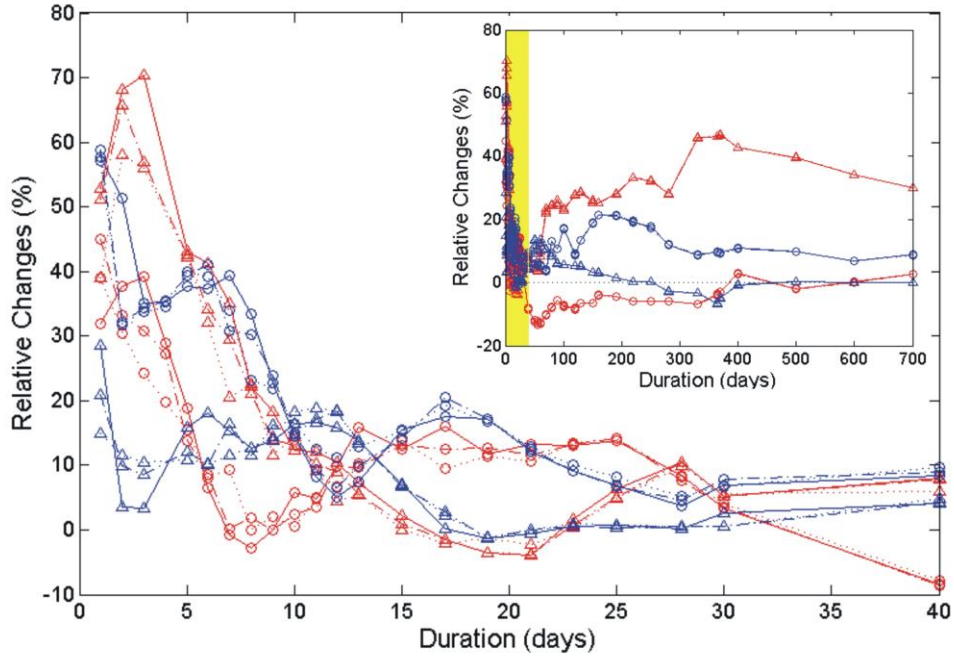
Figure 2.4: Same as figure 2.3, but also for the second (dashed lines) and third (dotted lines) maxima

2.4 Scaling properties and long lag correlation

2.4.1 Methods

Then, rescaled range analysis, structure function and power spectrum are applied to calculate Hurst exponent *H*.

Rescaled range analysis (R/S):

Hurst in 1951 introduced the R/S method, which is useful to measure some statistical aspects of the natural record in time, as discussed by Mandelbrot (1983) and Mandelbrot and Wallis (1969). RS analysis can be introduced as follow (Feder, 1988).

Given a time series {*X(t), t=1, ... , N*} at discrete time, the average over a period *d* is calculated as

$$< X >_d = \frac{1}{d} \sum_{t=1}^{d} X(t) \qquad (2.1)$$

A new variable *W(t)*, the so-called accumulated departure of the natural record in time from the average of *X*(*t*) over a period of *d* is given

$$W(t) = \sum_{k=1}^{t} (X_k - <X>_d) \qquad (2.2)$$

The range is defined as the difference between the maximum and minimum W:

$$R(d) = \max_{1<t<d} W(t) - \min_{1<t<d} W(t) \qquad (2.3)$$

Hurst found the natural phenomena, he studied, followed the empirical relation (R/S):

$$\lim_{d \to \infty} \frac{R(d)}{S(d)} \propto d^H \qquad (2.4)$$

Where $S(d)$ is the standard deviation of the cumulative-summed time series $W(t)$; and H is the Hurst exponent. By plotting $\log(R/S)$ versus $\log(d)$, one can obtain it as the slope of a straight line, in the scaling region.

Hurst exponent is a classical way to measure the persistence of a signal:

$0.5 < H < 1$ was taken to indicate persistence, while $H = 0.5$ indicates an uncorrelated process. $0 < H < 0.5$ indicates anti-correlation. To decrease fluctuation, the original time series is separated to several groups (depends on the sample size) of 2900 data sets and calculate the ensemble average of R/S.

Generalized Structure function:

For stationary processes, $X(t)$, a Structure Function of order q is defined as the q-th moment of the accumulated sum of $X(t)$:

$$S_{W,q}(d) = <(W(t+d) - W(t))^q> = <(\sum_{i=t+1}^{t+d} (X_i - <X>_i))^q> \qquad (2.5)$$

Where t denotes the t-th data point, and $<>$ denotes the ensemble average.

If the process $X(t)$ is scale-invariant and self-similar over some range of time lags $d1 < d < d2$, then the qth-order structure function is expected to scale as:

$$S_{w,q}(d) \propto d^{qH(q)} \qquad (2.6)$$

$H(q)$ is the Hurst exponent and identifies long-time correlation, as well as the stationary/non-stationary and mono-fractal/multi-fractal nature of the data. Practically, H is determined by the slope of $S_{w,q}(d)$ versus d on a log-log plot, which is equal to $qH(q)$. And q may be any real number not only integers.

Fourier spectrum:

The Fourier spectrum is a standard tool in fractal analysis, scaling regime classification and detecting long lag correlation of time series of variables (Harris et

al., 2001; Fraedrich and Larnder, 1993; Yano et al. 2004). Numerous studies have found evidence of scaling power spectra for rainfall in both space and time scales. The power spectrum density of a stationary process exhibits the power-law scaling:

$$\lim_{\omega \to \infty} F(\omega) \propto |\omega|^{-\beta} \qquad (2.7)$$

where ω is the frequency and β is an exponent that provides information on the scaling behavior of the field. The exponent β can be used as an indicator to characteristic time scales. When characteristic time scales are absence in a range of the power law, fluctuations within the range are scale-independent.

The relation between β and H is:

$$0 < \beta = 2H - 1 < 1 \qquad (2.8)$$

2.4.2 Results

To link rainfall at different time scales of aggregation, three methods namely R/S, generalized structure function, Fourier spectrum are employed to analyze the scaling regime and related long lag correlation.

The simulation with T31 resolution:

As Figure 2.5 shows, land records in full forcing millennium run are mainly composed of three rain spells from three single grid points, which are geographically next to each other over Bengladesh. Bengladesh is located in a tropical monsoon region in South Asia, north of Bay of Bengal and south of Himalayas and the Tibetan Plateau. It had three main seasons: a cool dry season (mid-October to the end of February), a hot summer season (from March to mid-May) and a wet monsoon season (late May to early October). With strong influence of monsoon, about 70% rainfall occurs between June and September. Notice, the single grid points, which are analyzed in this section, are all located in the Bengladesh. The maxima from the three single grid points in the simulation are marked as blue, red, green separately. The value of scaling exponent close to 0.7 can be found for the relationship between maxima and duration between more than 1 day and a few months respectively. The time series from the blue grid-point is analyzed and results are shown below.

As shown in Figure 2.6a, there are several evident peaks in the power spectrum, around 6 hours, 1 day, 3 months, 6 months, 1 year and 2 years respectively. The period ranging from 1 day to 3 months, which appears lack of characteristic time scales, has a declining slope (the bold back line) indicating with the power exponent

$\beta \approx 0.6$ or $H \approx 0.8$. Moreover, $H = 0.75$ is obtained by calculating the slopes of ensemble average of the R/S function in the lag range roughly between 2 days and 3 months (Figure 2.6b).
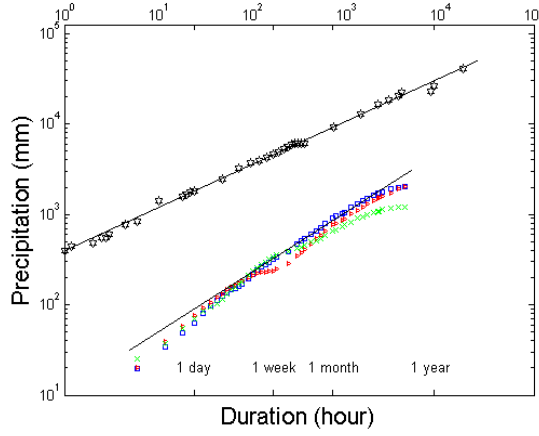
Figure 2.5: Maximum rainfall P versus time duration d in EH5OM (T31L19, from three land grid points)
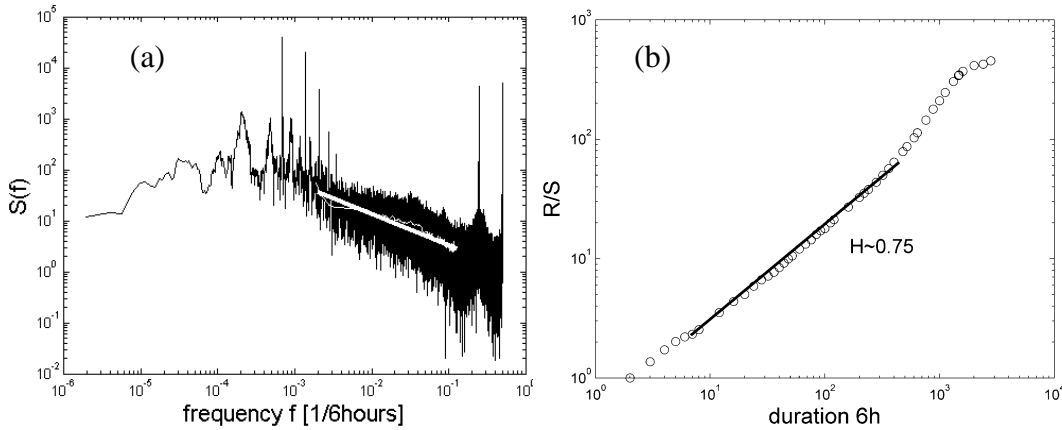
Figure 2.6: (a) Power spectrum versus frequency: the slope is the spectral exponent $\beta \approx 0.6 \Rightarrow H = (\beta+1)/2 \approx 0.8$ (b) Rescaled Range Analysis (R/S, ensemble average of 100 groups) versus duration d, the slope is $H \approx 0.75$ (from grid point data marked blue in figure 2.5)

In Figure 2.7, the qth order generalized structure function $S_{w,q}(d)$ of the accumulated data $W(t)$ are plotted versus aggregation interval d for q=0.5, 1.0, 1.5, …, 5.0 in the left plot. With the order goes higher, $S_{w,q}(d)$ represents more extreme rainfall events. Figure 2.7 clearly reveals the presence of different regimes (separated by dotted lines on the plot). The time scales, at which the scaling regimes break, are consistent with the peaks in Figure 2.6a, except for the missing 2-year time scale because of the limitation of aggregation intervals. Notice the time scales between 6

months and 1 year, $S_{w,q}(d)$ decreases with aggregation interval at higher orders, that indicates the period with no or rare rainfall extremes.

The scaling regime is roughly between less than 1 day and 3 months. This scaling range of time scales associate with variability of monsoon systems from synoptic scale to seasonal scale. The Hurst exponent of qth moment can be deduced from the slopes of the linear regression lines, whose value is equal to $qH(q)$, between 1 day and 3 months in left plot. Surprisingly, Hurst exponent decreases from 0.95 to 0.72 with increasing q. This indicates that: light rainfall varies as 1/f noise, and extreme rainfall events in this time range are also persistent correlated. When $q=7$, $S_{w,q}(d)$ should only represent the maximum rainfall event in all time scales; which implies $H(7)$ should be the same value as Jennings scaling exponent in the same time range, since $H(7)$ should be equal to the slope of $\log(P_{\max}^{q})$ versus $\log(t)\cdot q$ graph. And $H(7)$ is consistent with the scaling exponent b as 0.7. The results are in good agreement with those from the other two grid points.
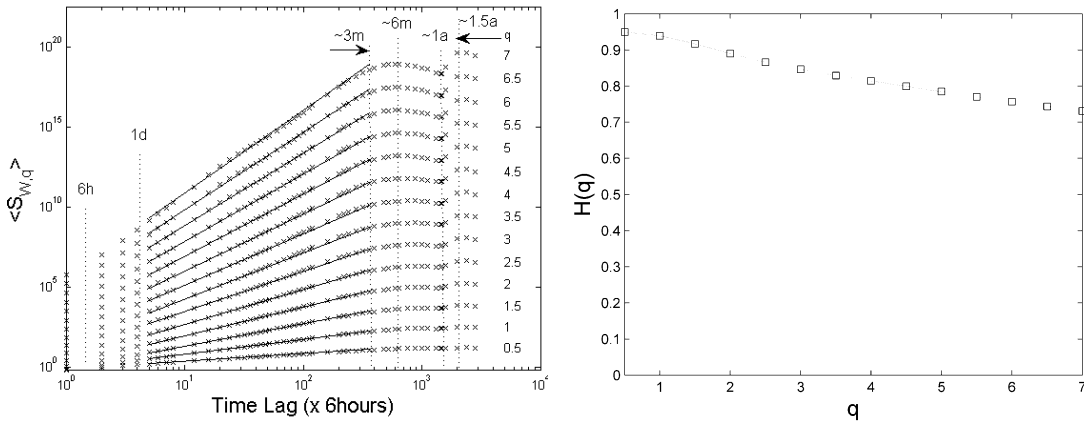
Figure 2.7: (a) Structure function, $S(d)$ of qth moments versus time lag for the grid point marked blue in figure 2.5. (b) $H(q)$ versus moments q

Analysis based on power spectrum, rescaled range analysis and the structure function shows long range correlation in the time series. Compared with the other two methods, generalized structure function offers several advantages: greater accuracy with almost no statistical bias, the absence of transition regions between different scaling ranges and identification of multi-fractal scaling in the data. Therefore, this method is exclusively used for later analysis.

Simulations with T63 resolution:

Land records in EH5OM (T63L31) are mainly composed of three rain spells from three single grid points, which marked red, blue, green (Figure 2.8a). The value of scaling exponent close to 0.6 can be found for the relationship between maxima and duration between more than 1 day and a few months respectively.

The generalized structure function $S_{w,q}(d)$ is plotted against aggregation interval d for different order q in Figure 2.8b. The first thing to be noted in the figure is that a scaling regime ranges from 4 day to 3 months. Beyond 3 months to 2 years, there are several other scaling breaks the same as in T31. The decrease of $S_{w,q}(d)$ with interval aggregating between 6 months and 1 year at all orders may be interpreted as a dry period.

The Hurst exponents of qth moment are deduced from the slope of the linear lines in Figure 2.8b: $H(q)$ decreases from 0.95 to 0.57 with increasing q (Figure 2.8c). $H(q=7)$ is approximately equal to its Jennings scaling exponent. The results are also in good agreement with those from the other two grid points.

Land records in EH6OM (RCP8.5)/ Hadley (RCP8.5) are mainly from two/ one rain spells from two/one single grid points. Analysis using generalized structure function shows similar results like that of EH5OM T63, shown in Figure 2.9 and 2.10; only with longer aggregation intervals, a break at around two-year scale can be found. For comparison, the same analysis is applied to a time series extracted from one grid point at (90E, 27N) in ERA-40; notice that the grid point is exactly located at the same region of Bengladesh like the previous grid points. The results are shown in Figure 2.11. The breaks at around 2 days, 5 months, 1 year and 1.5 years scales can be found. And $H(q)$ decreases from 0.92 to 0.51 when the order increasing; which implies light rainfall are highly correlated, the correlation decreases in stronger rainfall events, until zero for the most extreme ones (white noise).

2.5 Summary and discussion

The ability of global climate models to reproduce extremes on different time scales is of great importance for climate estimates of the past and the future. Therefore, the comparison with observed functional relationships is useful to verify model performance. The maximum rainfall-duration scaling-law relationship: $P = P_0(d/d_0)^b$, $b \approx 0.5$; which has been observed at land stations to hold over a wide duration range, is the basis for the verification analysis of two state-of-the-art global (grid-point and spectral) climate models. The main results can be summarized as follows:
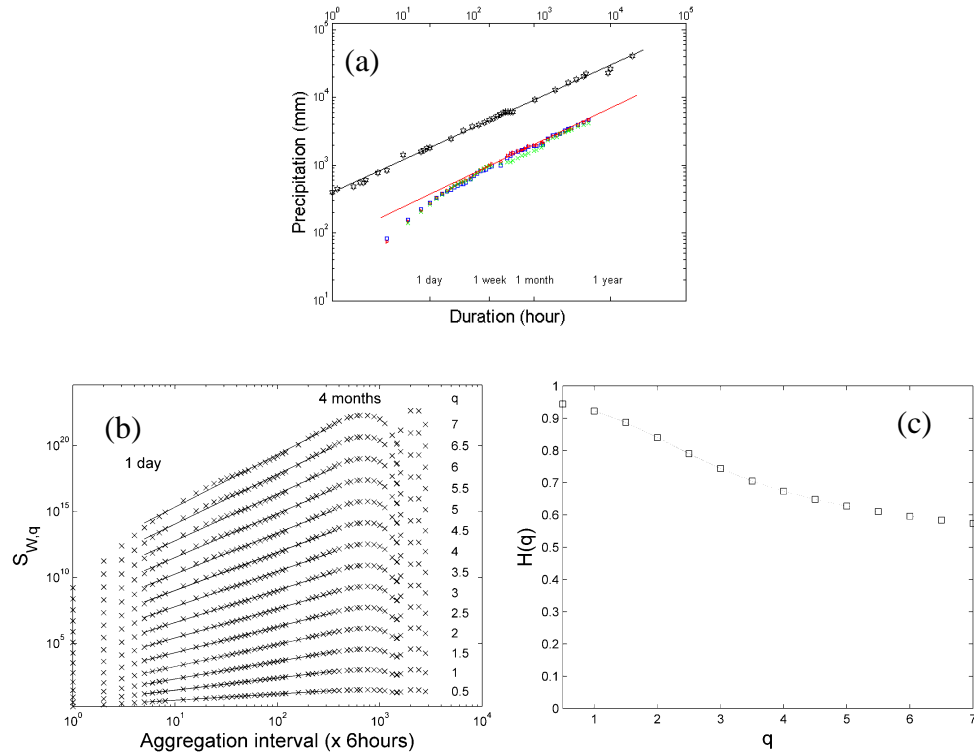
Figure 2.8: (a) Maximum rainfall P versus time duration d in EH5OM(T63L31). (b) Structure function, $S(d)$ of qth moments versus time lag for the grid point data in blue. (c) $H(q)$ versus moments q
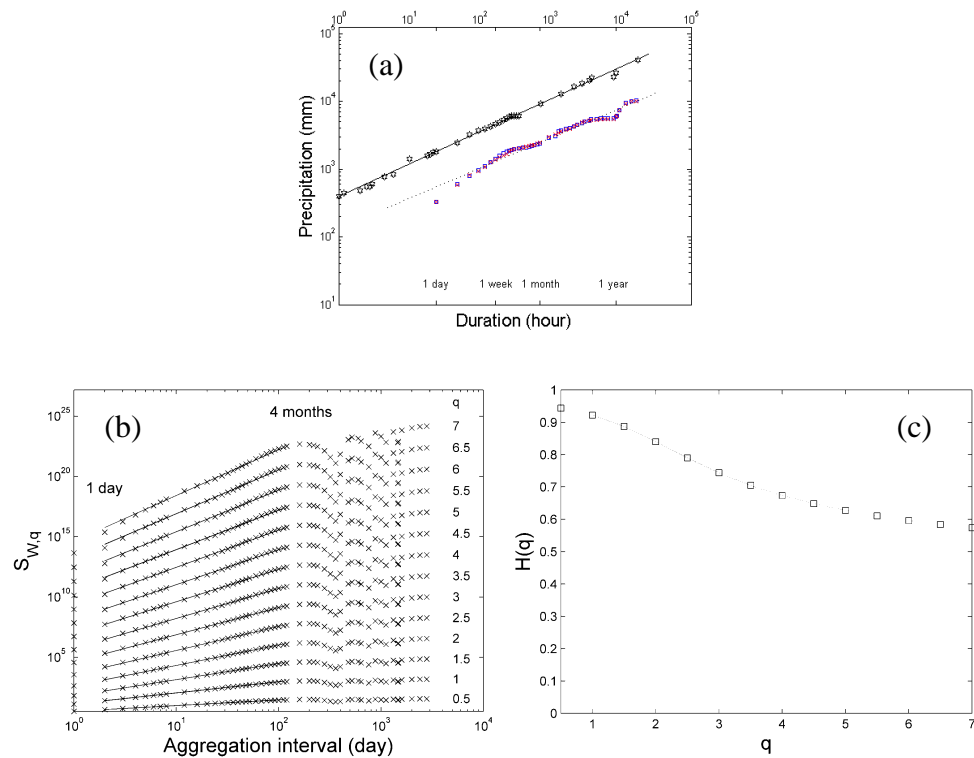
Figure 2.9: As in figure 2.8 but for EH6OM (RCP8.5)
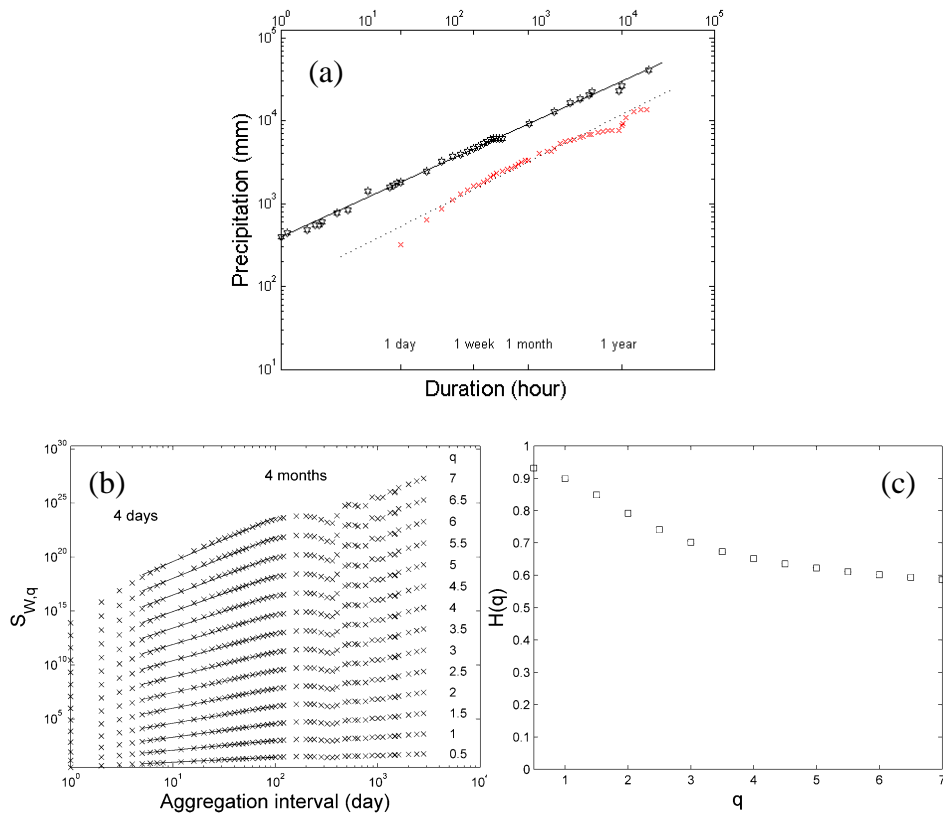
Figure 2.10: As in figure 2.8, but for Hadley (RCP8.5)
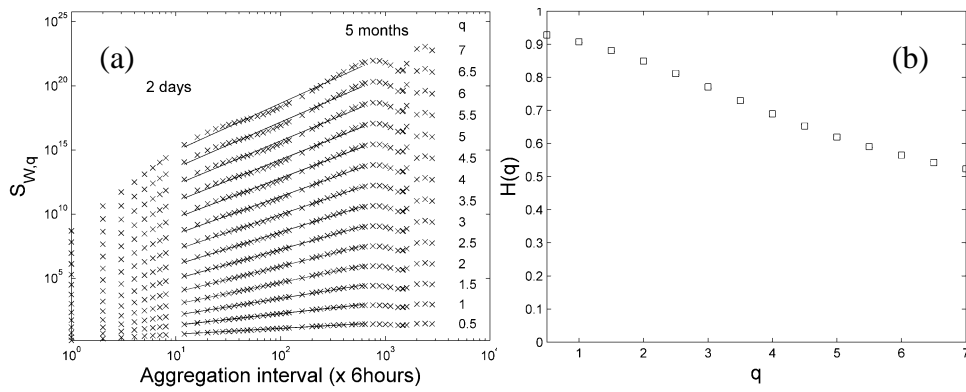
Figure 2.11: (a) Structure function, $S(d)$ of qth moments versus time lag for the grid point at (90E, 27N) in ERA-40. (b) $H(q)$ versus moments q

i). Jennings scaling law for the world's maximum rainfall is found in model data covering a wide range of scales with three orders in magnitude (compared to six orders in observations). The scaling exponent $b \approx 0.5$ is found at both land and ocean grid points (which is also observed at land stations). The lower resolution model follows a larger scaling exponent $b \approx 0.7$. Furthermore, second and third maxima show similar behavior. The analysis of Jennings maximum rainfall depth-duration scaling law in global climate models may provide guidance for cascade dependent bias correction not only for the first maxima but also for general extreme rainfall events.

ii). The simulated rainfall extremes (T31L19 resolution) are about one order of magnitude smaller than the observed ones; this difference is reduced for models with enhanced spatial resolution. Magnitudes of rainfall maxima increase in general with higher resolution (EH5OM, T63L31) but the increments are higher over land than over ocean. In the warmer climate (RCP8.5) the intensity in the maximum rainfall events increases by about 50% for durations of days, but vanishes for monthly time scales.

iii). In high resolution simulations (T63L31), the scaling law is composed of rain spells of short duration occurring at different locations, while rainfall extremes of longer durations (> 5 days) are located at few grid points and generated by few extreme spells.

iv). The scaling phenomenon for time scales longer than one day is related to the existence of scaling regime. The increase of scaling exponent b from 0.5 to 0.7 (with increasing resolution) may indicate a random process modified by enhanced persistence (Zhu et al., 2010). Employing the generalized structure function analysis (Harris et al., 2001) to the 6-hourly time series at those grid points which contribute to the maxima selected for Jennings scaling law (from T63L31 to T31L19 resolution) lead to the Hurst exponents as a measure of autocorrelation or persistence.

v). 1/f noise is found in light rainfall in a specific Asia monsoon area in all simulations and ERA-40.

Revisiting Jennings law using ERA-40 reanalysis:

Jennings scaling law is also revisited using ERA-40 data covering the period from 1957 to 2012. The scaling exponent as 0.7 is found for first (Figure 2.12a), second and third maxima. The same exponent value is found in T31 simulation previously. The assimilation model used for the ERA-40 data has a horizontal spectral resolution

of T159 and L60 height level. Why the maxima scaling is similar as the one in the low resolution (T31) simulation? The locations of the maxima are plotted in Figure 2.12b, except the maximum record at 12 hours originates from Asia monsoon region, the others are scattered in tropical continents or islands. This phenomenon is contradictory with both the observations and simulations. The reason may be related to excessive tropical oceanic rainfall after 1991, which is also considered as one of the most serious problems in ERA-40 (Uppala et al., 2005).

Time series from one grid point, which contributes the maxima roughly between 2 days to 20 days, is analyzed by generalized structure function (shown in Figure 2.12c). Rainfall events in the time range (6 hours ~ 15 days) are persistent correlated, Hurst exponent varies between 0.82 and 0.72 (Figure 2.12d). For most extreme events, the correlation is calculated as 0.72, which is consistent as its Jennings scaling exponent, as expected.

Disappearance of scaling in the transfer regime:

As mentioned in the introduction of this chapter, scaling records for durations shorter than 3 days are scattered over the tropics and subtropics, in a wide range of longitudes and latitudes. Why can the scaling law not originate from a single station like those records at longer time scales?

Generalized structure function analysis is again employed to analyze a rainfall time series, collected by the TOGA/COARE research vessel Kexue with resolution of 1 minute covering the period from November 1, 1992 to March 3, 1993. Together with rainfall, several other variables from the dataset have been assessed by Yano et al. (2004). They found existence of clear $1/f$ spectra in temperature, humidity, and wind speed, but not in rainfall. Later $1/f$ noise has been found in binary time series of rainfall by Blender et al. (2011).

As shown in Figure 2.13, the multi- order moment structure function as a function of scale show inner scaling regime ($<$ 10 min), transfer regime (between 10 min and 27 hours) and scaling regime ($>$ 27 hours). The boundary between the inner and the transition regime may be located 10 ~ 15 min, and between transition and scaling regimes 20 ~ 80 hours, depending on site and season (Marini, 2003; 2005). The transition regime can not be described by a simple power law scaling. For $q = 0.5$, the existence of scaling lasts the whole scales, and $H(0.5) = 0.95$ (close to $1/f$ noise). And the existence of transition regime between around 10 min and 27 hours gives an explanation for records for shorter time scales from different stations. But how those records in Jennings figure generate a scaling relationship is still unknown.
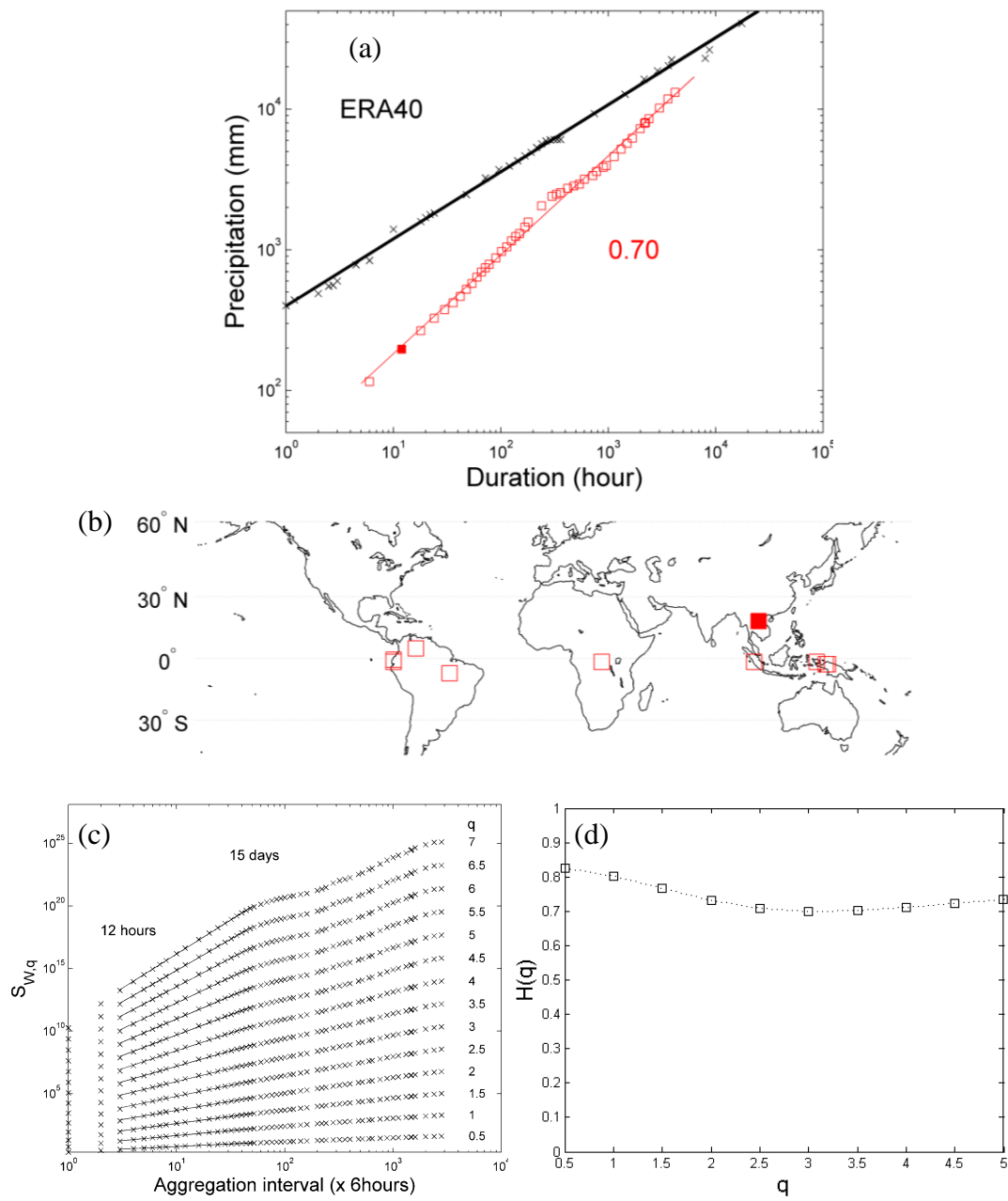
Figure 2.12: (a) Maximum rainfall-duration diagram from observed station data (black) and ERA-40 reanalysis data over land (red); and thin solid lines indicate linear fits. (b) Geographical locations of maxima records in ERA-40, symbols are the same as in (a). (c) Structure function, $S(d)$ of qth moments versus time lag for the grid point on Indonesia island. (d) $H(q)$ versus moments q
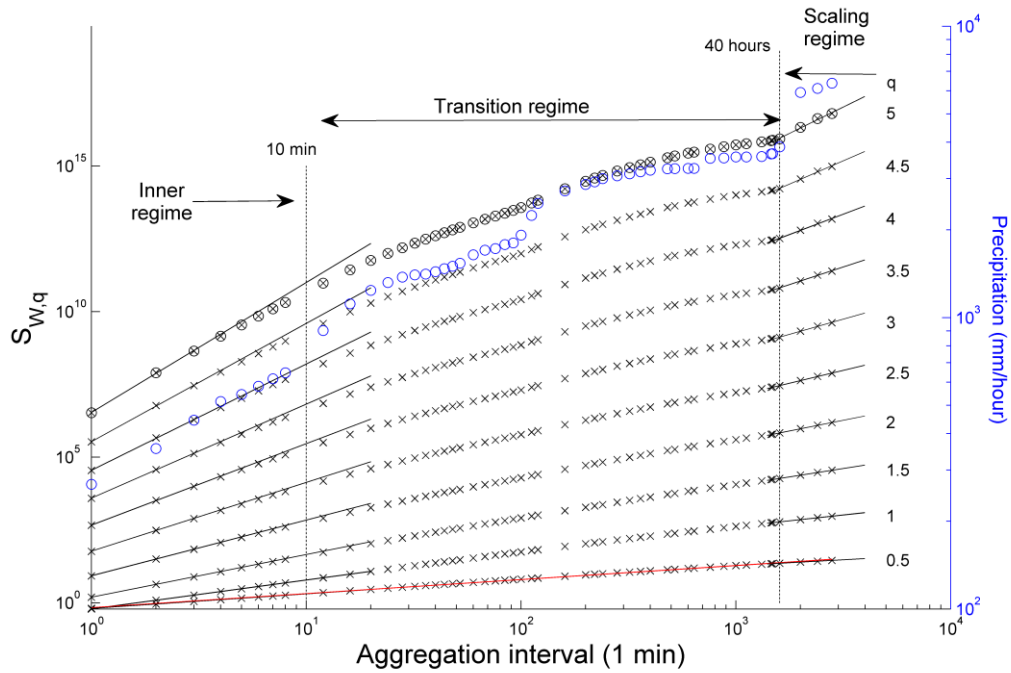
Figure 2.13: Maximum values versus duration for Kexue (blue circles); and structure function, *S*(*d*) of qth moments versus time lag. *qH*(0.5) is the slope of the red linear line in the log-log diagram: *H*(0.5) = 0.95

Chapter 3

A conceptual model: scaling of rainfall extremes

Section Summary

The observed relation of worldwide rainfall maxima P versus duration d follows Jennings scaling law, $P \sim d^b$, with scaling coefficient $b \approx 0.5$. This scaling is demonstrated to hold for single station rainfall extending over three decades. A conceptual stochastic rainfall model which reveals similar scaling behavior is introduced as a first order auto-regressive process AR(1) to represent the lower tropospheric vertical moisture fluxes, whose upward components balance the rainfall while the downward components are truncated and defined as no-rain. Estimates of ERA-40 vertical moisture flux autocorrelations (at grids near the rainfall stations) provide estimates for the truncated AR(1). Subjected to maximum depth-duration analysis, the scaling coefficient, $b \approx 0.5$, is obtained extending for about two orders of magnitude, which is associated with a wide range of vertical moisture flux autocorrelations $0.1 < a < 0.7$.

3.1 Introduction

Rainfall maxima, which are the sole subject of Jennings law, always refer to certain accumulation time scales, covering duration up from minutes to 2 years. This is a scaling law of extremes (first maxima) and not of the variability as described by variance density in a log-power/log-frequency plot or related functions in the time domain. On time scales of a few days, the local thermodynamics certainly play a determining role; beyond a few days, weeks, months, other large-scale physical factors enter. A prominent example is the Cherrapunji station in India, which is presumably related to the fact that it is in the reign of the Asian summer monsoon in a unique topographic setting and rain-bearing systems like tropical and midlatitude cyclones.

So far, only two papers have commented on this scaling; Hubert et al. (1993) connected the scaling exponent to a singularity parameter by employing multi-fractal methodology, while Galmarini et al. (2004) proposed a combination of the rainfall distribution with a time-lag autocorrelation thereby covering scaling ranges of about three decades of duration. As a parsimonious theoretical concept of the Jennings law, scaling of maximum rainfall depth versus duration has not yet been introduced.

The modeling of daily rainfall data is one challenging subject because the methodologies which can be successfully applied to continuous time series generally fail to presence the intermittences (no rain days). Since daily rainfall data is a basic climate dataset and an important input for modeling hydrologic impact, several methods were designed to generate daily rainfall. Generally, those methods or say generators can be classified into four groups, and a detailed review is given by Srikanthan and McMahon (2001). Most common models of daily rainfall are based on Markove chains to simulate the relation between the current day state and one- or several preceding days. The order of the Markov chain determines the number of preceding days. The optimum order of Markov chain model may be required differently depending on the location and during the time period of the year. But a general conclusion is that a first-order model normally is adequate (Jimoh and Wenster, 1996, 1999). Various literatures have considered first order (two states, rain and o rain day) Markov models (Gabriel and Newmann, 1962; Caskey, 1963; Weiss, 1964; Feyerherm and Bark, 1965, 1967; Lowry and Guthrie, 1968; Selvalingam and Miura, 1978; Stern, 1980; Richardson, 1981; Stern and Coe, 1984; Hannachi, 2012). To solve the deficiency in this approach, the lack of probably embedding intermittences, a truncated first-order Markov chain model (namely, truncated AR1), has been applied to model daily rainfall (Kelman, 1977; Hannachi, 2012). The censored AR(1) process is widely used as a simple and effective method to generate

rainfall, as Hannachi (2102) demonstrated in a simulation producing rainfall data in Armagh/Northern Ireland. Truncated AR(1) basically is a truncated normal probability distribution, and its probability density function has been estimated by Cohen (1959). In this analysis, the simple conceptual model is employed, the censored (or truncated) AR(1) process, to simulate Jennings scaling law observed in rainfall data. In this study, the positive values of a first order autoregressive process represent the vertical moisture flux in the lower troposphere.

Jennings scaling law is revisited focusing on the scaling behavior of single station rainfall observations (section 3.2). Section 3.3 introduces the conceptual stochastic model of rainfall and its maximum rainfall depth-duration scaling analysis. Section 3.4 provides conclusions.

3.2 Jennings scaling law over continental China

When reanalyzing the Cherrapunji (India) daily rainfall time series, Dhar and Farooqui (1973) found that the time span for maximum rainfall depth-duration scaling ranges from one day to two years. Therefore, scaling law holds also for single stations lying in the Jennings scaling line. Along this line, it will not be surprising to find similar maximum rainfall-duration scaling at other stations, but the extent of the scaling regime may vary. This hypothesis is tested with daily rainfall time series at 732 basic weather stations over China (1951‒2008, provided by the National Climate Center, China Meteorological Administration).
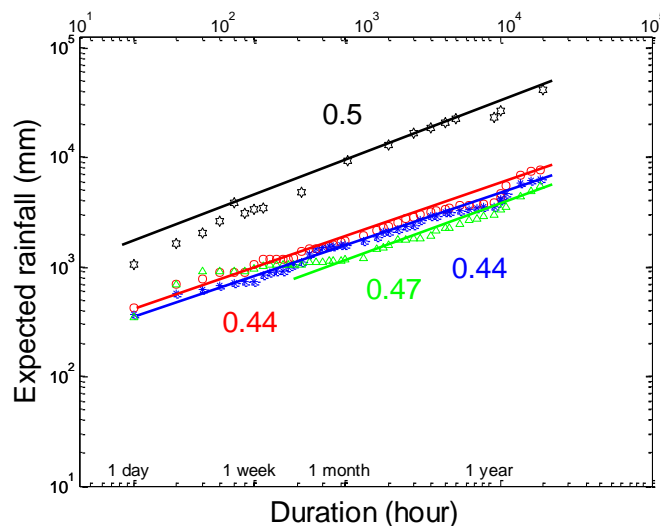
Figure 3.1: Maximum rainfall-duration scaling diagram: Cherrapunji (India, pentagrams, $b \approx 0.5$), Lushan (green triangles, $b \approx 0.47$), Dongxing (red circles, $b \approx 0.44$) and Fangcheng (blue stars, $b \approx 0.44$).

The maximum accumulated rainfall data from 1 day to 2 years are extracted (Figure 3.1): shorter term records ($\leq$ 6 days) are from Shangchuandao (1 day), Yangjiang (2 days) in Guangdong and Lushan (from 3 to 6 days) in Jiangxi province (in central China). Longer term (> 6 days) records are mainly from Fangcheng and Dongxing in Guangxi province. As shown in Figure 3.1, the maximum rainfall depth-duration relation is observed in the selected single station records with the scaling exponent $b \approx 0.5$. Notice that the scaling exponent b remains constant for the second and the third maxima, which can be considered as the maxima found in a shorter time series. This means that the value of the scaling exponent close to 0.5 is stable with respect to the record length of rainfall data. Thus Jennings scaling law appears as a more general scaling rule governing single station rainfall depth-duration extremes. In the following, we introduce a conceptual model to simulate the scaling-behavior in single station data.

3.3 A conceptual model

In a qualitative sense, moisture which is supplied by surface evaporation and lateral convergence in the lower layers of the troposphere sustaining the vertical moisture flux, provides the water source for rainfall in the case of upward moisture flux (associated with the meso- to synoptic and larger scale airflow dynamics) and governs the dry episodes of zero rain when a downward moisture flow or zero motion is favored. Therefore, a time series of vertical moisture flow may be a suitable surrogate for a rainfall time series, if we assume, for simplicity, that only upward vertical moisture flux is proportional to rainfall rate while subsidence characterizes the zero-rainfall or dry phases. This is a basic mechanism of rain-bearing synoptic scale systems ranging from tropical cyclones and monsoonal depressions to the mid-latitude disturbances often characterized as slant-wise convection. The vertical upward motion is relevant for convection and stratiform rainfall, which are embedded in and usually forced by the developing low pressure systems of synoptic scale with and without being effected by topography.

Here we introduce a parsimonious surrogate model for rainfall to describe the maximum depth-duration scaling following three steps: (i) A first order autoregressive process AR(1) is introduced as a surrogate of vertical moisture flux time series at locations near the rainfall stations analyzed in Figure 3.1. (ii) This surrogate AR(1) moisture flux time series is truncated to keep only upward fluxes representing rainfall sequences at a single station. (iii) In the end, the truncated surrogate moisture flux time series is subjected to maximum rainfall depth-duration scaling analysis. The moisture flux data are derived from ERA-40 datasets (European Centre for Medium-

-Range Weather Forecasts reanalysis; 1.125-degree grid, 1958 to 2001; Uppala et al. 2005).

Vertical moisture flux – an AR(1) process: Based on ERA-40 datasets daily vertical moisture fluxes in the lower troposphere

$$m(t) = w(t)\, q(t) \qquad (3.1)$$

are calculated, where w represents the vertical velocity and q the mixing ratio. ERA-40 grids are chosen to include those rainfall stations exhibiting Jennings scaling law (Figure 3.1, note Fangcheng and Dongxing are located in the same grid). The first order autoregressive process AR(1) with discrete time steps t and Gaussian random noise r (mean as u and variance as σ^2)

$$m(t) - u = a(m(t-1) - u) + r \qquad (3.2)$$

is characterized by the lag-1 autocorrelation a; it corresponds to an integral time scale, $\tau \approx \sum_{i=0}^{\infty} a^i \cong 1/(1-a)$, as a suitable measure for the memory of the underlying process (see for example, Fraedrich and Zielmann (1994) on surrogate predictability experiments based on the first order autoregressive process AR1). Figure 3.2 shows the lag-1 autocorrelation coefficients of water flux anomalies in the lower troposphere at the selected grids and their AR(1) processes. Notice that, for Fangcheng and Lushan, most maximum rainfall events happen during the rainy season. Therefore we use the water vapor flux data in rainy season to reduce seasonal fluctuations. All of them show short term memory (less than 4 days), which leads to the respective AR(1) processes. The next step is to treat an autoregressive process as a surrogate of the sequences of positive and negative moisture fluxes (or "updraft versus subsidence").

Rainfall – a truncated AR(1):

Rainfall rate $R(t)$ can be estimated to be proportional to the vertical flux of moisture:

$$R = E\, w\, q, \quad w > 0 \qquad (3.3)$$

where $w > 0$ is the ascent rate, and E is the rainfall efficiency which is defined as the ratio of the mass of water falling as rainfall to the influx of water vapor mass into the cloud and supposed constant (see for example, Doswell et al. 1996). Then the total rainfall is formalized as $p = R \cdot t_d$, with the rainfall duration t_d. Based on this premise, we assume a proportionality between the amplitude of the daily moisture updraft $m(t)$

and the expected value of daily rainfall *p(t)*, the surrogate rainfall time series –
suitable for statistical analysis – is simply given by the positive values of the moisture
flux *m(t)>0,* while the negative values *m(t)<0* represent zero rainfall.

$$p(t) = \begin{cases} E \cdot m(t) & w > 0 \\ 0 & w \leq 0 \end{cases} \quad for \quad \qquad (3.4)$$

where *E* is a constant for rainfall efficiency and supposing *E* = 1 in our analysis; both
units of *p* and *m* are mm/day. This model generates a truncated stochastic time series
which is based on a continuous autoregressive process to model intermittent
phenomena (see Hannachi (2012) for a comprehensive analysis, application and
review). The choice of short-term memory and autoregressive type stochastic models
for rainfall surrogates has been substantiated further by observed scaling properties of
daily rainfall records (see for example, Fraedrich and Larnder, 1993; Fraedrich et al.,
2009).
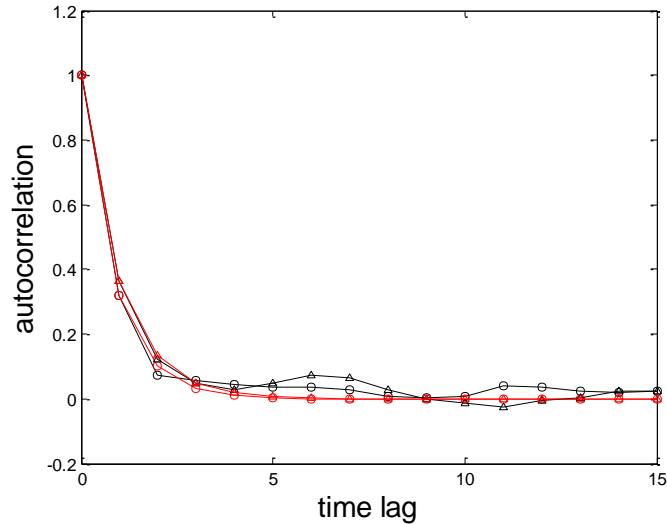
Figure 3.2: Autocorrelation functions (full lines) of 850hpa vertical water fluxes
anomalies at grids close to the following stations (black) and their first order
autoregressive processes (red): Lushan (triangles, a ≈ 0.36), and Dongxing and
Fangcheng (circles, a ≈ 0.31).

Maximum rainfall depth-duration scaling for a truncated AR(1):

An example of an AR(1) process is shown in Figure 3.3a for the station
Fangcheng/Dongxing (*a ≈ 0.31*) where the positive part represents upward water
vapor flux or rainfall intensity. Figure 3.3b shows the associated maximum rainfall
depth-duration scaling (or Jennings scaling law) suggesting a power law exponent

close to $b \approx 0.5$, which last from days to three months. Due to the limited length of the rain season here, the duration cannot be longer than four months. The mean of expected rainfall in Fangcheng is 51.1mm/day, compared to 11.9 mm/day in the observations; the standard deviation of expected rainfall is 55 mm/day, compared to 30.3 mm/day in the observations. The same analysis has also been done for station Lushan ($a \approx 0.36$, Figure 3.4). The mean of expected rainfall in Lushan is 32 mm/day, while 7.1 mm/day for the observed in the rain season; and the standard deviation of expected rainfall is 39 mm/day, while 21 mm/day for the observed in the rain season. The average and variance of the rainfall in Fangcheng is higher than in Lushan. Since the rainfall efficiency cannot be 100%, the magnitudes of simulated rainfall are much higher than that of the observed ones. AR(1) processes are capable to reproduce the Jennings scaling law in single stations.

Supposing the moisture flux is a zero-mean, unit variance AR(1) process ($\mu = 0, \sigma = 1$), equation (3.3) becomes

$$m(t) = a \cdot m(t\text{-}1) + r \qquad (3.5)$$

the maximum rainfall depth-duration relation is extracted from the positive part of this truncated AR(1) process. As shown in Figure 3.5, the Jennings scaling law with power law exponent close to $b \approx 0.5$ covers about two orders of magnitude. Note that the power law scaling does not change substantially for different coefficients $0.1 < a < 0.7$. However, for larger integral time scales (for example $a = 0.999$) the power law slope increases to $b \approx 0.8$. The results stay robust for second and third maxima. In this sense we may interpret the Jennings law' scaling as an outcome of an AR(1) process. The calculations above are based on a constant efficiency, $E = 1$. Calculations for varying E, and with shorter memory show that the scaling exponent does not change: we ran a simulation with a 'weakly' stochastic E with seasonal long memory:

$$E(t\text{+}1) = A \cdot E(t) + 0.05r \qquad (3.6)$$

where $E(1) = 0.7$; $A = 1 - 1/90 = 0.99$, since 90 days are a season; and r: random noise with mean 0 and variance 1.

The result shows the scaling exponent 0.5 for $0.1 < a < 0.7$ (Figure 3.6). Therefore, the efficiency E does not have to be a constant. E with a reasonable variation does not change the scaling exponent.
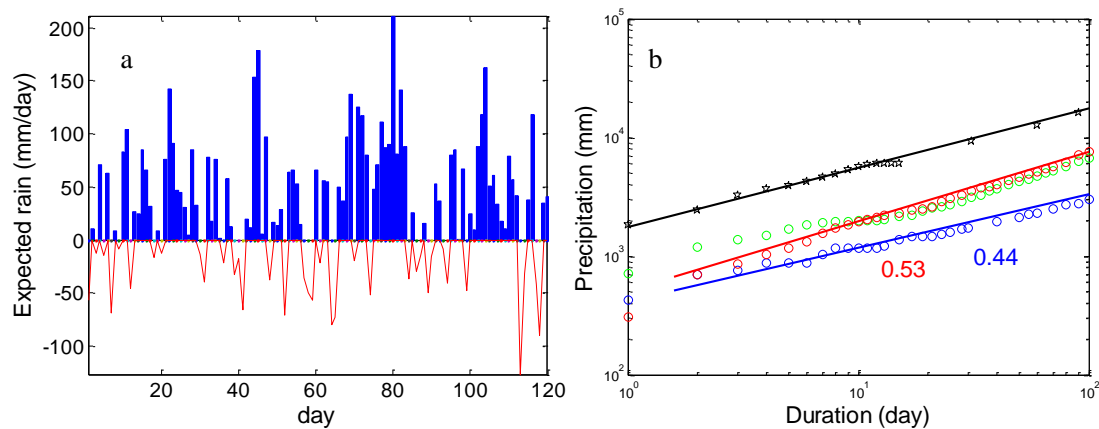
Figure 3.3: (a) Snapshot of a first order autoregressive process time series at station Fangcheng (AR(1) with $a \approx 0.31$) with positive ranges marked blue. (b) Simulated maxima rainfall (red circles) versus duration relationship by the positive parts of AR (1) processes at Fangcheng station. Blue circles: observed maxima; Green circles: the expected rainfall; Black Pentagram: world records.
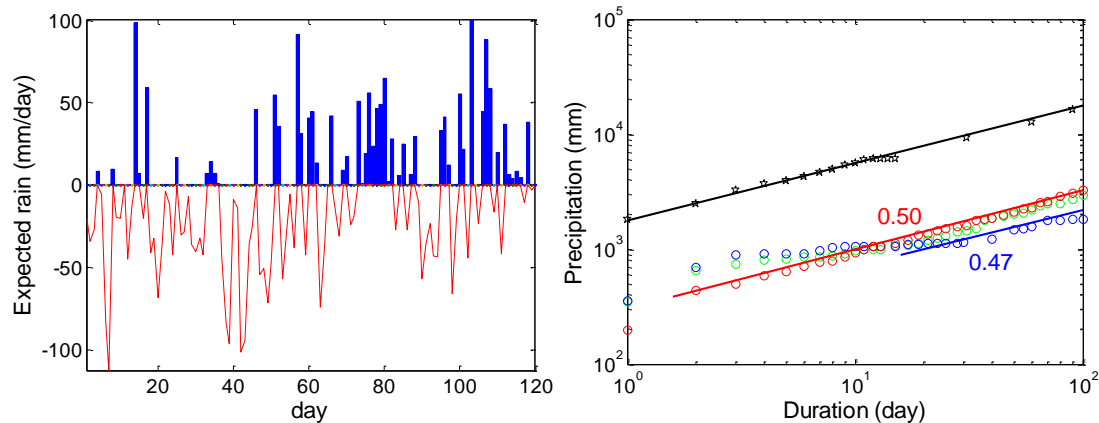
Figure 3.4: Same as figure 3.3 but for the station Lushan (AR(1) with $a \approx 0.36$)
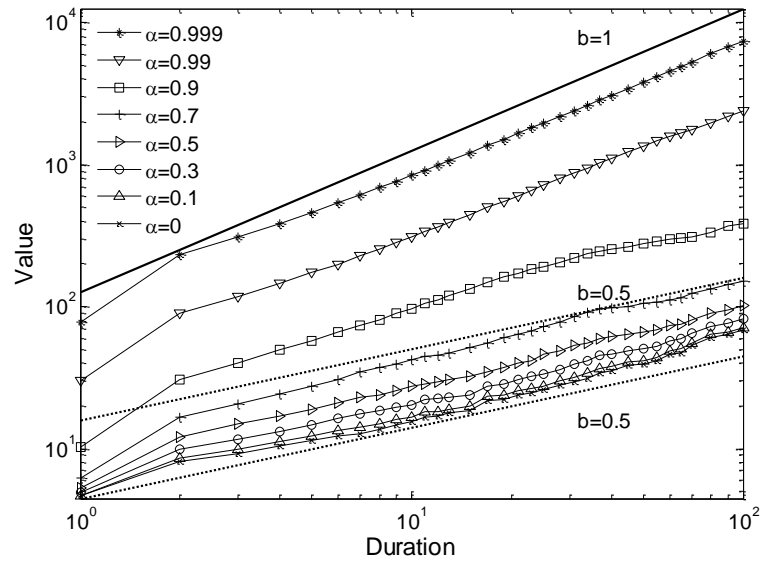
Figure 3.5: Simulated maximum rainfall versus duration relationships obtained by the positive parts of AR (1) processes with different coefficients *a* as indicated (total length 10^6 time steps). The dotted and solid lines denote the exponent *b = 0.5* and *b = 1*;
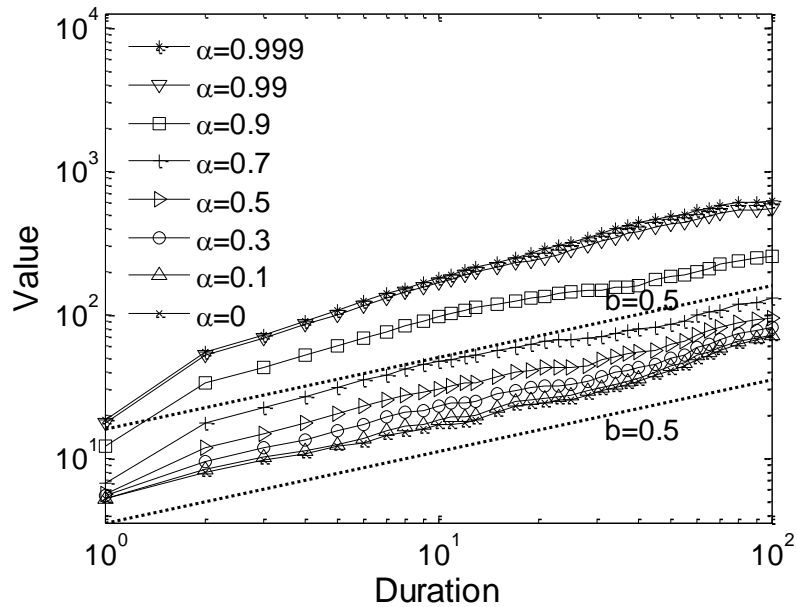
Figure 3.6: Same as figure 3.5 but *E* with weak memory

3.4 Summary and discussion

The Jennings scaling law, $P \sim d^{\,b}$ with $b \approx 0.5$ has been revealed from a worldwide ensemble of rainfall observations (Jennings 1950). The finding has been substantiated for three decades of the scaling regime when the analysis is confined to daily rainfall records (taken from China's basic weather stations). As a concept for such station related maximum rainfall depth-duration scaling behavior, a truncated (censored) first order autoregressive process is introduced, which has recently also been used to simulate daily rainfall times series in mid-latitudes (Hannachi 2012). Here we provide the physical censor to truncate the downward episodes of an AR(1)-process for the case of downward lower troposphere moisture fluxes. The remaining upward-only moisture flux time series, sustaining the rainfall events, describes the rainfall intermittency and shows the scaling behavior of the maximum rainfall depth-duration following Jennings scaling law as observed at single rainfall stations.

In this sense, we have introduced the dynamics behind the underlying the first order autoregressive process as a surrogate model for atmospheric water fluxes; and by implementing the censorship truncating the downward fluxes, only the positive (upward) fluxes are kept and thus intermittent, which leads to the nonlinear scaling behavior documented by Jennings scaling law.

Chapter 4

Daily-scale rainfall extremes and related dynamics (a case study)

Section Summary

In this chapter, dynamic processes which lead to daily scale extreme rainfall events are investigated. Extreme Value Distribution (EVD) is employed to identify warm season (MJJAS) rainfall extremes over continental China using both observations and Global Climate Model (GCM, MPI-ESM) simulations. The spatial patterns of extreme rainfall using simulations of present-day conditions are compared with observations. An extreme value Point Process (PP) model is fitted to MJJAS extreme daily rainfall with index presenting Western Pacific Subtropical High (WPSH). That is, WPSH is covariate of one or more parameters of the PP model. Results show that WPSH statistically significant influences on extreme rainfall in vast regions except south China. A high phase of WPSH, indicating the subtropical high extend more westward and has a stronger intensity, corresponds to a substantially increased likelihood of extreme rainfall over north China, but a decreased likelihood of extreme rainfall over southern China and the northern border of northeastern China. The influence of WPSH on extreme rainfall over China in simulated climate is also analyzed. Changes of the distribution of extreme rainfall are investigated under climate change.

4.1 Introduction

The expected changes of extreme rainfall events under climate change have attracted considerable research efforts in the last years, mainly due to the occurrence of floods and the related damages (see for example, Benestad, 2006; Kattsov et al., 2007; Holman, 2012). The potential of changes of extreme events is likely to vary at a much higher rate than changes of the total rainfall under global climate change (Karl and Knight, 1998; Kunkel et al., 1999; Groisman et al., 2005; Alexander et al., 2006; and Trenberth, 2011). Since the 1990s, extreme weather/climate events in China happen frequently, especially extreme rainfall events, which caused floods in 1998 and 2008 in southern China.

The space and time variability of the rainfall over China is very complicated, dominated by the East Asian Summer Monsoon (EASM). The beginning of the rainy season, the jumps of the rain belt and summer rainfall anomalies are all closely related to the shift and intensity of the EASM. The northward progression of EASM is closely associated with the variation of the Western Pacific Subtropical High (WPSH). The WPSH tends to expand and strengthen during boreal summer. The two seasonal abrupt northward migrations of the WPSH in March–July characterize three different month-long rainfall periods over China, namely the pre-Meiyu period, the Meiyu period and the post Meiyu period. The two jumps of the WPSH normally happen in mid-June and late July, or sometimes in August: the first jump signals the beginning of Meiyu in the Yangtze River valley, Japan, and Korea; the second jump the WPSH shift to its most northern position, signals the end of the Meiyu and the start of the rainy season in northern and northeastern China. The distribution of summer rainfall in China is associated with the east-west movement and the strength of the WPSH. Overall, the location and intensity of the WPSH determine the area, where, in the warm season, warm and humid air from the lower latitudes meets the cold and dry air from mid to high latitudes. In addition, both zonal and meridional changes of the WPSH exhibit also interannual to decadal variations, which have a pronounced connection with the interannual to decadal scale changes of the EASM. Since the late 1970s, the WPSH has extended westward, which has resulted in a rain-band shift over China, with excessive rainfall along the middle and lower reaches of the Yangtze River valley and deficient rainfall in north China (Hu et al., 2003; Yu and Zhou, 2007). Therefore, if the WPSH is well predicted, it could establish a promising way for the EASM rainfall (Wang et al., 2013).

Relating the WPSH, a large-scale atmosphere circulation, with smaller-scale variables, in our study extreme rainfall at a single station can be used for downscaling (Katz et al., 2002). Instead of dynamic downscaling usually by employing Regional Climate Models (normally at very high costs of computer consumption), a statistical

approach is used which is easy to understand and inexpensive. For exceptional and rare events, Extreme Value Distributions (EVD) have been widely used to play the bridge (Katz et al., 2002; Kharin and Zwiers, 2005; Wang and Zhang, 2008). In detail, based on maximum likelihood estimation, the Generalized Extreme Value (GEV) distribution, Generalized Pareto distribution (GPD) and return values with embedded covariates contribute substantially to quantify potential changes of climate extremes under anthropogenic forcings, to indicate an influence of large-scale circulation patterns on the occurrence and distribution of extreme events. This study is an attempt to link downscaling with statistics of extreme daily rainfall events over China based on EVD.

Coupled General Circulation Models (CGCMs) are the state-of-the-art tools to simulate present-day climate and future scenarios, and provide long-term data for the analysis of extreme events (IPCC, 2007). However, most models only poorly simulate heavy rainfall events (Durman et al., 2001; Alexander, 2009; Zhang et al., 2013), especially in the subtropics (Kharin et al., 2013). In this analysis, the spatial pattern of extreme rainfall is compared with the observed one over China. The influence of WPSH on extreme rainfall is also analyzed.

The study is organized as follows. Section 4.2 gives information about the observation data and model simulations, used for the analysis and the WPSH indices. Section 4.3 concentrates on the methodology of the applied PP model for stationary and non-stationary processes. The results of our analysis are shown and discussed in section 4.4. In the last section, the results are summarized and an outlook is given for possible future studies.

4.2 Data and indices of Western Pacific Subtropical High

Observation and reanalysis data:

The daily rainfall dataset is provided by Climate Data Center (CDC) of the National Meteorological Center of the China Meteorological Administration, including 732 observation stations in mainland China. Only warm season data covering the period between 1959 and 2005 are used in this analysis. The data were subjected to quality control in the CDC. Temporal inhomogeneity, caused by station relocation, is screened out, when the location (or the elevation) of the rain gauge experienced a change of more than 20 km (50 m) (Zhai and Ren, 1999). As some inhomogeneities may still remain, this imperfection of the dataset is acknowledged. Stations with too many missing values are dropped: a year is considered to be missing if there are more than 10 days missing rainy daily in MJJAS; a station is considered only when > 25 years of valid observations (non-missing values) are available. Ultimately, 483 stations passed this quality control, and most of them are located in eastern China.

The monthly values of the 500hpa geo-potential high from 1959 to 2005 are extracted from the National Centers for Environmental Prediction - National Center for Atmospheric Research (NCEP-NCAR) reanalysis dataset (Kalnay et al. 1996; Kistler et al. 2001). A climate shift in the mid-to-late 1970s has been detected in this dataset (Trenberth and Hurrell 1994). A change in the surface station or increased urban heat island effect has been stated as a possible reason.

Model data:

The GCM simulations used in this analysis are performed by state-of-the-art coupled ocean-atmosphere general circulation models: MPI-ESM (mainly includes ECHAM6 and MPIOM) with a spectral atmosphere. The model is being developed by the MPI-M (Max Planck Institute for Meteorology) participating in the CMIP5 runs. A detailed description of ECHAM6 is given by Stevens et al. (2013). ECHAM6 is run at T63 resolution ($\approx 1.9° \times 1.9°$) with 47 vertical levels up to 10Pa. The ocean model MPIOM has a horizontal grid spacing of about 1° with 40 unevenly spaced vertical levels. This analysis particularly concentrate on the warm season (MJJAS) daily rainfall in two 47-year time slices in this study. The first is taken from the present climate simulation ranging from 1959–2005 (referred to as 20C). The second time slice, ranging from 2153–2199, is taken from the rising radiative forcing period of the Representative Concentration Pathway 4.5, which are named after a continuous rise in radiative forcing during the 21st century leading to $4.5 \mathrm{Wm}^{-2}$ in the year 2100 (hereinafter referred to as RCP4.5).

WPSH indices:

The WPSH is usually represented by a specific closed isoline of the 500hPa (or 850hpa) geopotential height, for example, the extent of the 5880 geopotential meter (gpm) at 500hpa. Most former studies of the WPSH are base on a series of indices published and updated by CMA in *Meteorological Monthly,* including the intensity (the "volume" of WPSH over 5880 gpm), the ridge (the latitude of the central axis position), the north margin (the average latitude degree of the north margin of the 5880 gpm contour) and the west boundary (the minimal longitude degree of the 5880 gpm contour).

Except these indices, a variety of interrelated WPSH indices have also been used (Lu, 2002; Yang and Sun, 2003; 2005; Sui et al., 2007; Wu and Zhou, 2008; Wang et al., 2013). Here we use the monthly indices defined by 500 hPa geopotential height (Z500) anomaly averaged over 10°N–30°N, 120°E–140°E. A detailed description is given by Sui et al., 2007. The correlation between Sui's WPSH index (hereafter

referred to as WPSH) and the indices from CMA is given in Table 4.1. This WPSH index is significantly correlated with the western boundary and intensity of the subtropical high. Therefore, a high phase of WPSH may indicate the subtropical extends more westward and has stronger intensity.

Table 4.1: Correlations between the index from Sui et al. (2007) and indices from CMA, numbers in bold type are statistically significant

Correlation	Ridge	West boundary	Intensity	North margin
WPSH	-0.2	**-0.468**	**0.668**	-0.12
Ridge		0.054	0.068	**0.937**
West boundary			**-0.6**	0.002
Intensity				0.06

4.3 Methodology

In early time, some fixed thresholds were used in China to define extreme events: rainfall greater than 25mm/day is defined as heavy rainfall, greater than 50mm/day is storm. But obviously, it failed to describe the extreme rainfall in dry areas, for example, rainfall intensity as high as 10mm/day can cause landslide. This fixed threshold method also cannot describe "extreme rainfall events" in dry season (normally in winter). Internationally, thresholds in percentage are broadly used. Here the 90 percentile of rainy day events during 1959–2005 is used for each station as an extreme event criterion.

4.3.1 Extreme Value Distributions

Supposing in a given series of maxima, taken over a certain time block are M_1, M_2, …, M_n, according to Fisher-Tippett Theorem (Fisher and Tippett, 1928), there exist sequences of constants $a_n > 0$ and b_n:

$$\Pr(\frac{M_n - b_n}{a_n} \leq z) \rightarrow G(z) \quad n \rightarrow \infty \qquad (4.1)$$

G(z) follows the Generalized Extreme Value (GEV) distribution which can be described by:

$$G(z) = \exp(-[1 + \xi(\frac{z - \mu}{\sigma})]^{-\frac{1}{\xi}}) \qquad (4.2)$$

with the parameters: location μ , scale σ and shape ξ; and $\sigma > 0$, $1+\xi(\frac{z-\mu}{\sigma}) > 0$. ξ determines the three types EVD: Frechet $\xi > 0$, Gumbel $\xi = 0$ (interpreted as the limit case $\xi \rightarrow 0$), and Weibull $\xi < 0$.

In our case, the warm seasonal rainfall maxima can be directly fit into the GEV model (1) through maximum likelihood or other statistical techniques. But the estimated parameters can be very inaccurate when the length of the time series is short. But here we have only 6000 samples at most while, for some stations only less than 3000 samples (excluding missing values) are available to calibrate the model. One alternative method could be the peaks-over-threshold (POT) method. A well defined threshold is selected, and the data exceeding the threshold can be fit into the Generalized Pareto Distribution (GPD). GPD works better than GEV because more values are incorporated in estimating the distribution. The parameters of GPD can be deduced by the corresponding GEV distribution, but not vice versa (Coles, 2001; Katz et al., 2005). And the scale parameter has to be adjusted to the choice of the threshold.

But in this study, another alternative approach is adopted: a Point Process (PP) model. The PP approach is used to describe the occurrence of extreme rainfall events in warm seasons, whose value is over the sufficient large threshold u. Following the convention, a fixed 90% percentile threshold is taken at each station; notice that, to prevent not really extreme rainfall events to be taken into account in *dry* regions (especially in the northwestern China), the threshold is defined as the 90% of all observed rainy days at each station.

With the extracted extreme values X_1, …, X_n, with $y = X_i - u > 0$ and threshold u, a non-homogeneous Possion process with intensity measure on A= $[t_1, t_2] \times (y, \infty)$ is given by

$$\Lambda(A) = (t_2 - t_1)(1 + \xi \frac{y - \mu}{\sigma})^{-\frac{1}{\xi}} \qquad (4.3)$$

The advantage of the PP model is that the parameterization is in terms of the GEV parameters, and these parameters are normally better estimated because more values fitting into the model are extracted. And the scale parameter σ is invariant to threshold in contrast to that of the GPD model. Therefore, the PP model can be used for non-stationary effects by including time or covariates in the parameters, because of the invariance of all parameters to the threshold.

Parameter estimation:

Parameter estimation is performed based on the maximum likelihood method. The basic method of estimation is therefore to choose the parameters (μ, σ and ξ) to minimize the negative log-likelihood.

Goodness of fit:

To check whether the extreme rainfall data can be well fitted by PP, a Kolmogorov-Smirnov (KS) test (Stephens, 1970) is applied. This test measures the overall differences between two (cumulative) distribution functions: the empirical distribution function estimated from extreme rainfall samples and its theoretical distribution. When the maximum difference exceeds a certain critical value, the hypothesis is rejected, that the theoretical distribution can not represent the observed extremes.

Since the theoretical distribution is unknown, a parametric bootstrap procedure is applied to obtain the significance levels for the distribution of difference, (e.g., Kharin and Zwiers, 2000; Sillmann et al., 2011). First, a random series with the same size of observed extremes are generated from each fitted PP, and a difference is derived from each generated sample. Secondly, repeat the first step for 1000 times. The 5th quantile of the differences is employed as the critical value for the rejection of the null hypothesis at the 5% significance level.

Return values:

The N year return levels X_N are estimated by:

$$X_N = u + \frac{\sigma'}{\xi}[(Nn_y k_u / n)^\xi - 1], \quad \xi \neq 0 \quad (4.4)$$

Where $\sigma' = \sigma + \xi \cdot (u - \mu)$, n_y is the number of rain days per year; k_u is the number of extreme rainfall days exceeding u; and k_u/n represents the exceedance probability.

4.3.2 Point Processes model for non-stationary processes

Predictor variables may be incorporated into the PP model by expressing the location and scale parameters as functions of the predictors. The shape parameter is usually taken as a constant. Because the scale parameter needs to be positive, a log transferred scale parameter is used:

$$\begin{cases} \mu = \mu_0 + a \cdot X \\ \ln(\sigma) = \sigma_0 + b \cdot X \\ \xi = \xi_0 \end{cases} \quad (4.5)$$

where X is a predictor variable. In the following, the model without a predictor (M_0) is called the stationary model. In this case, the covariates have no influence on the

parameters of the distribution. The coefficients *a, b,* represent the effect of the predictor on the PP, for models with only one covariate (*a*) in location parameter (M_1), or only one covariate (*b*) in scale parameter (M2), or two covariates (*a, b*) in location and scale parameters respectively (M3) are called non-stationary models.

Notice, in the likelihood function, μ and σ are taken in the form presented in (5),

depends on the regression coefficients μ_0 and σ_0, *a* and *b*. They can be estimated

using the Maximum Likelihood (ML) method to find the minimum of *–log(L)*, with PP model parameters. The collection of models (M_0, M_1, M_2 and M_3) mentioned above, where one or two parameters of the PP model are conditioned on WPSH, are summarized in Table 4.2. The degree of freedom (dof) for each model corresponds to the number of parameters in the respective PP model.

Table 4.2: The PP models for the stationary case (model 0) and the non-stationary cases (model 1, 2, 3), where one or two parameters are conditioned on WPSH and their corresponding degrees of freedom (dof)

Model	PP model parameters	Dof
0	μ_0 ; σ_0 ; ξ_0	3
1	$\mu_0 + WPSH \cdot a$; σ_0 ; ξ_0	4
2	μ_0 ; $\sigma_0 + WPSH \cdot b$; ξ_0	4
3	$\mu_0 + WPSH \cdot a$; $\sigma_0 + WPSH \cdot b$; ξ_0	5

Model selection:

To avoid over-fitting and to test for significant improvement of higher dimensional statistical models, Akaike's information criterion (AIC) is applied (details in Akaike, 1974). For small-sample bias adjustment, AIC is calculated following Hurvich and Tsai (1989):

$$AIC = -2\log[\mathcal{L}(\hat{\theta} \mid y)] + 2K(\frac{n}{n-K-1}) \quad (4.6)$$

With maximized Likelihood, $\mathcal{L}(\hat{\theta} \mid y)$, number of estimated parameters, K, and the multiplier, the correction factor *n/(n-K-1)*.

From a set of models with AIC_j (model number j), the best model is the one with the minimum value AIC_{min}. Akaike differences (Δ_j) are calculated to rank and compare the models

$$\Delta_j = AIC_j - AIC_{min} \qquad (4.7)$$

While $\Delta_j < 2$ gives models with strong, $4 < \Delta_j < 7$ considerably less and $\Delta_j > 10$ no support.

$$w_j = \frac{\exp(-0.5\Delta_j)}{\sum_{j=1}^{J}\exp(-0.5\Delta_j)} \qquad (4.8)$$

gives the possibility of the model j is the best one.

4.4 Results: extreme rainfall events and Western Pacific Subtropical High

4.4.1 The distribution of rainfall extremes and its relationship with WPSH in observations

Distribution of extreme rainfall (stationary model):

The stationary PP model is employed to fit daily extreme rainfall observation data in warm season over China. The method of maximum likelihood is used through to estimate the three parameters (location, scale and shape); 458 out of 483 stations passed the goodness of fit check. Figure 4.1 shows the results: a distinct northwest-southeast gradient of the three parameters can be seen, with higher (lower) values of location and scale parameters in the southeastern (northwestern) China (Figure 4.1a, b). Notice that, in northwestern China occur obvious biases because data are available only from a few stations. This gradient reflects the overall spatial rainfall pattern in China with abundant rainfall and higher variability in southeastern China, and a lack of rainfall in northwestern China. The shape parameter is generally positive, indicating a Frechet distribution (Figure 4.1c). The RV20 (Figure 4.1d), which can be used to infer measures for flood protection, combining the information of the three individual PP model parameters, also reveals a northwest-southeast gradient with lower (higher) return values in northwestern (southeastern) China. Notice, RV20 varies largely by region: the maximum return values in the southeast can be twice as large as the smaller ones in the northwest.
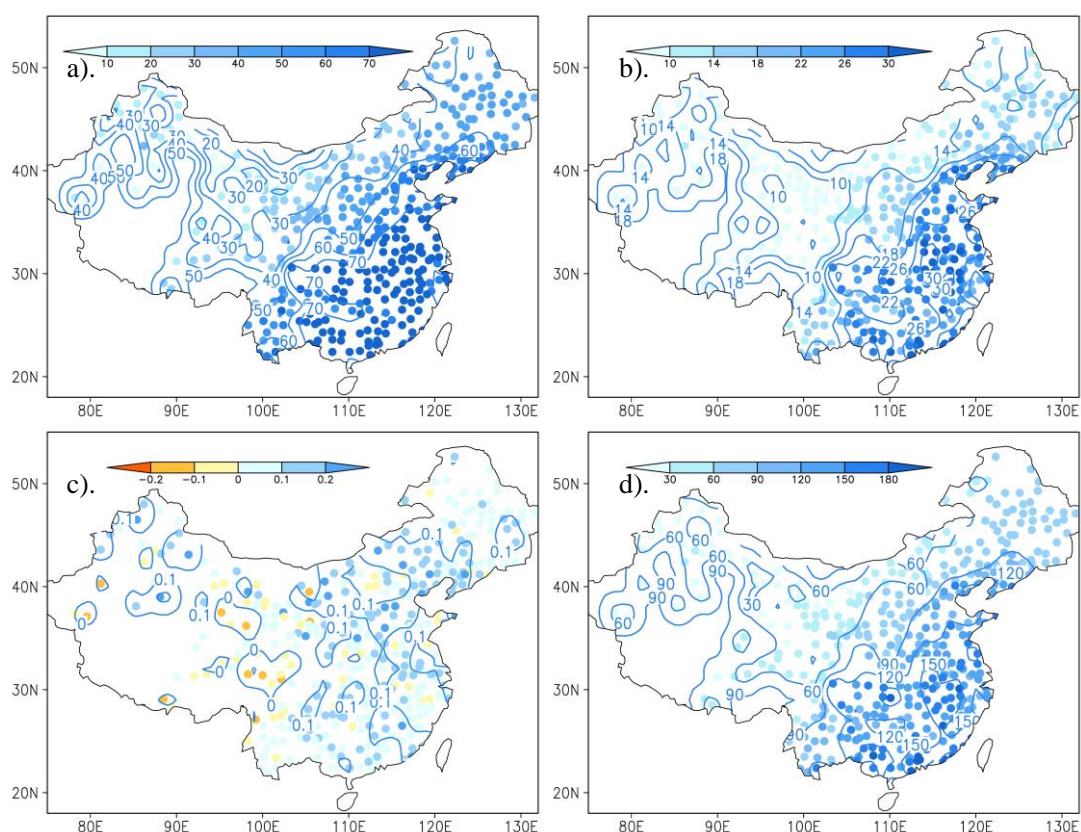
Figure 4.1: Parameters of PP distribution: location (a), scale (b), and shape (c) for the observed daily extreme rainfall for the period of 1959–2005; 20-year return values (RV20, d) are calculated based on the three parameters. Stations where the KS test failed are not shown.

Trends of extreme rainfall (non-stationary model):

Under climate change, extreme rainfall may exhibit trends. To investigate the temporal trend in extreme rainfall events, time is used as a predictor variable in non-stationary models (M1, M2 and M3) to allow the location, or scale, or both parameters to vary linearly. For each station, the best model is selected with AIC criteria which take into account the numbers of parameters and the negative maximized log-likelihood (nllh) associated with each model (Figure 4.2). The estimate of the coefficient (*a*) of the location parameter is also shown in Figure 4.2 to give an impression of the phase of the trends. The location parameter of extreme rainfall distribution has a positive trend in Northwest and Southeast China, a negative trend in North China in the last 50 years. Few stations, however, do not satisfy the non-stationary model, that is, their trends are not significant. This finding is consistent with trends of R95 (annual total rainfall of top 5% rainfall) over China using another statistical method (see You et al., 2011).
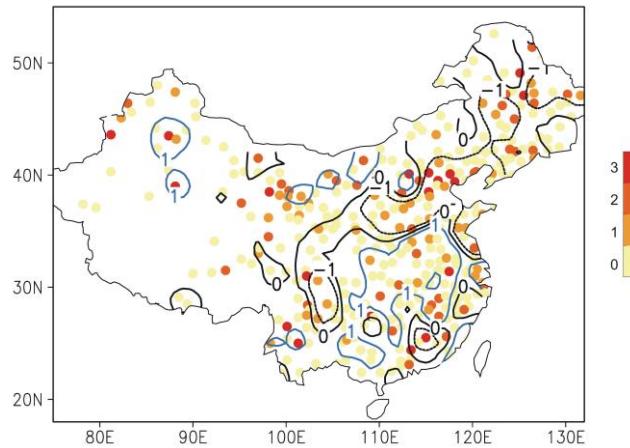
Figure 4.2: Trends of distribution of observed extreme rainfall: implanting time as a covariate in the location (M1), scale (M2) and both location and scale (M3) parameters of the PP model respectively; and best model selected with the AIC criteria (M0: the stationary model). Solid lines: the corresponding slope of the location parameter.

Influence of WPSH on the distribution of extreme rainfall events

(non-stationary model):

The regional mean of the 500 hPa geopotential height within 10°N – 30°N, 120°E – 140°E is used to quantify the interannual variability of the WPSH (Sui et al. 2007; Wu and Zhou, 2008). As shown in Figure 4.3a, this area is one center of the standard deviation of summer (JJA) mean geopotential height at 500 hPa for the reanalysis.

To understand how changes in the large-scale circulation affect extreme rainfall, WPSH is included as a covariate into the PP model of daily extreme rainfall at each station. A collection of models are set up, including the stationary model without covariate, and non-stationary models where one or more parameters of the PP model are linked to WPSH. Then AIC is employed to choose the best one model with significant improvement at each station. As shown in Figure 4.3b, except for a small area in southeastern China, most parts agree with the non-stationary model (M_j, $j \geq 1$) being selected as the best model. Thus, the large-scale factor WPSH significantly influences the extreme rainfall over China. Notice that, South China overall is not influenced by WPSH, because a considerable amount of rainfall is caused by tropical cyclones (in some years up to 30% of total warm season's rainfall). The blue (black) lines indicate the positive (negative) slope of the location parameter in model 1. When WPSH is in a high phase, the location parameter of the extreme rainfall distribution tends to increase at most stations with model 1 as best model.
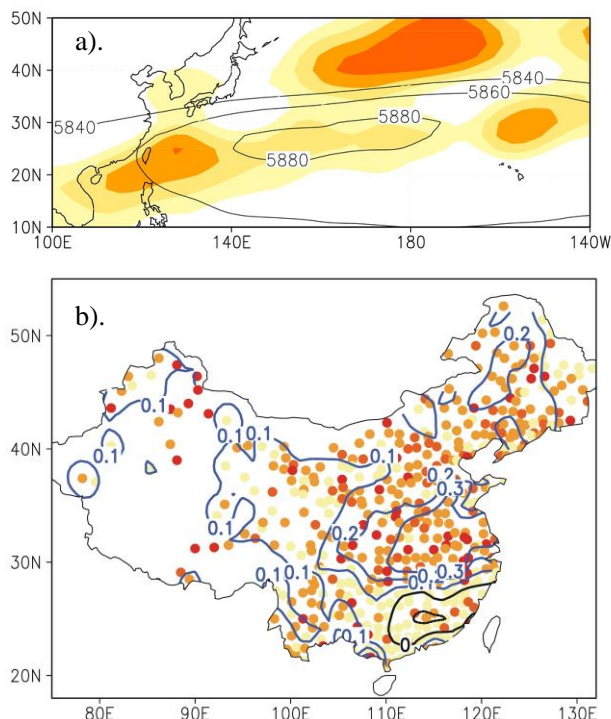
Figure 4.3: (a) Contours represent climatological 500 hPa geopeotential height (Z500) of the reanalysis and shading denotes spatial distribution of standard deviation of Z500 calculated by 2–5 year band pass filtered data normalized by zonal mean value. (b) The same as figure 4.2 but using WPSH as the covariate.

One goal of this analysis is to construct the empirical relationship between the large-scale factor WPSH and local extreme rainfall. Based on this relationship, the changes of WPSH may be expected to project the changes of the 20-year Return Value (20RV) over China under climate change conditions. Observation data from 1959–2005 are used to calibrate the relationship. An obvious trend in the time series of WPSH can be found in Figure 4.4a. To show the ability of the non-stationary PP models to "predict" the changes of extreme rainfall with respect to the changes of WPSH, mean anomalies of WPSH in two different periods (1959–1979 and 1980–2005) are used to generate projections of the changes of RV20; and then compared with the deviations of RV20 calculated from fitted stationary PP model in the two periods. As shown in Figure 4.4, the projected relative changes of 20-yr return value of extreme daily rainfall have similar patterns as the observed ones: decrease in north China, increase in Southern China and at the northern border of northeast China, but generally the intensity of changes is underestimated, which is not surprising because of the variations of WPSH.
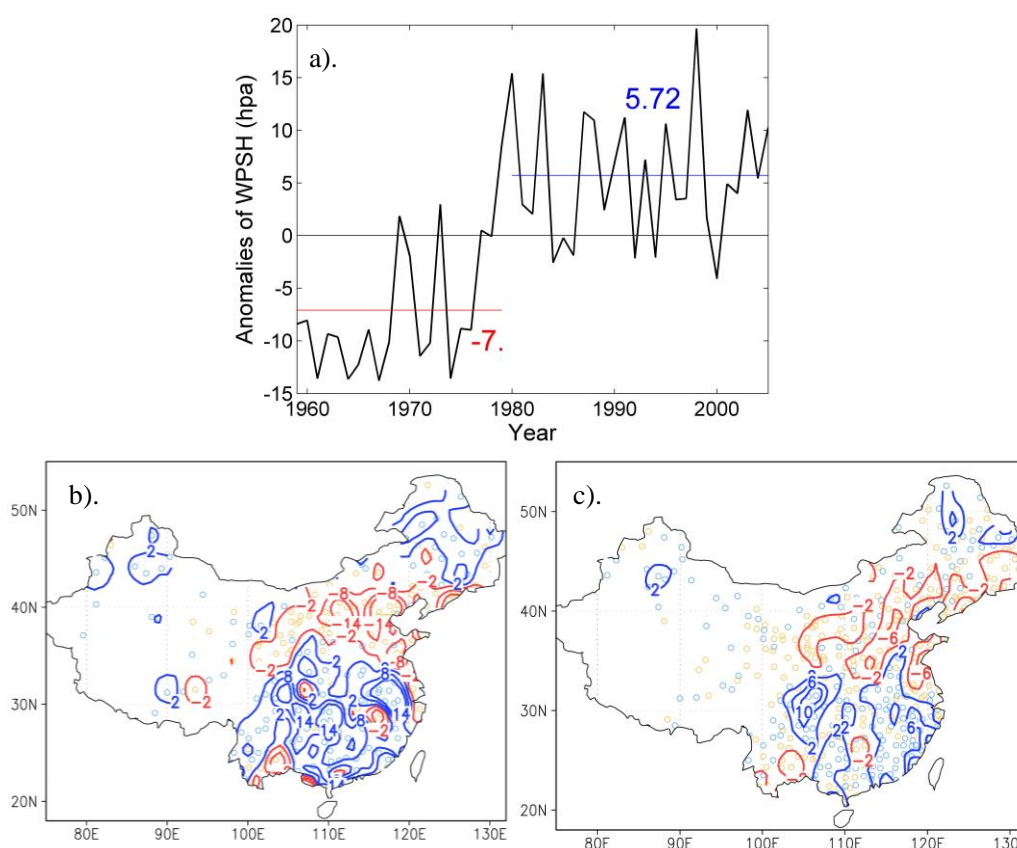
Figure 4.4: (a) Time series of WPSH anomalies with respect to the mean value during 1959–2008; (b) the deviation of 20RV of extreme daily rainfall in 1980–2008 vs. 1959–1979 and (c) PP model projected changes of 20RV with WPSH anomalies varying from 5.72hpa to -7hpa.

4.4.2 The distribution of rainfall extremes and its relationship with WPSH in simulations: present and future

Distributions of extreme rainfall events simulated by GCMs in

present-day (stationary model):

The same method as before is used to fit stationary PP model to 20C daily warm season extreme rainfall and the results are compared with the observed data.

As shown in Figure 4.5, there is a general agreement between the spatial patterns of the location and scale parameters, and the 20-year Return Value (RV20). There are also differences: for example, the observed maxima of RV20 are located in the south-

east coastline and, in parts, mid and -lower Yangtze region, but inside two river valleys in middle China for 20C; also the center which is over the southern and eastern edges of Tibet for 20C is not observed. This is possibly due to the horizontal resolution which does not enable an accurate representation of the topography along the southern and eastern edges of Tibet, and shows a fake high rainfall center; and this is also found by Wang and Yu (2013). Not surprisingly, the location and scale parameters of the PP model fitted to the 20C simulations are lower (around 20mm less) than the ones observed (Figure 4.5a and 4.5b), because the model simulated extreme rainfall is normally interpreted as an areal (grid-point) mean of extremes. Different from observations, the shape parameter for 20C is mostly negative indicating a Weibull distribution (Figure 4.5c); this may significantly contribute to the severe underestimation of RV20 in 20C (Figure 4.5d), which is half as strong as the observed one.
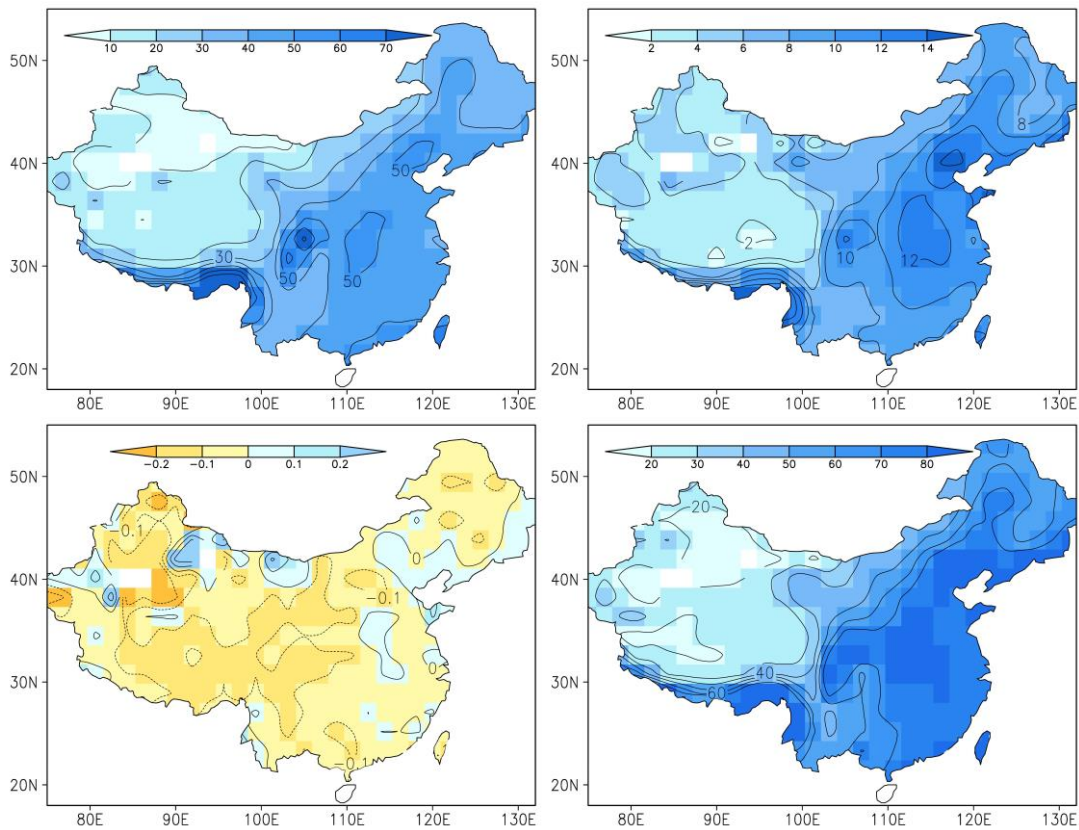
Figure 4.5: Same as figure 4.1, but for ensemble mean of 20C members: calculating the parameters and RV20 using each simulation then calculate the mean.

Influence of WPSH on the distribution of rainfall extremes in present-day simulations:

All simulation ensemble members can reasonably reproduce its location of the isoline of 5860 gpm (representing the WPSH), but with relatively weaker intensity, which leads to slightly shifting the western edge and center to the northeast (compared to reanalysis). The locations of interannual variability centers (the standard deviation of JJA mean geopotential height at 500hpa) of WPSH are generally well reproduced but with different strength in all the ensemble members.

Again, a collection of models are set up, where one or more parameters of the PP model are linked to the WPSH (Figure 4.6). In 20Cs simulations a large area over southern Tibet, two river regions and southeastern China agree with the non-stationary model, in which WPSH is implanted as a covariate only in the location parameter, being selected as the best model; this implies WPSH significantly influences extreme rainfall events in those regions. The pattern of impact of WPSH on extreme rainfall is similar to the one in observations: positive in eastern China without the southeastern coast area. However, the influence of WPSH on extreme rainfall is much weaker in simulation than observed comparing the impact area or the slope of the location parameter (*a*). This may be related to the WPSH being weakly simulated in 20Cs. Therefore, significant trends in extreme rainfall can be found in some regions in 20Cs simulations comparing with observations.

Influence of WPSH on the distribution of rainfall extremes in a future climate:

The location of WPSH in the future RCP4.5 is similar as in 20Cs, as shown in Figure 4.7. However, its intensity significantly increases compared to the ones in 20Cs. The interannual variability centers of WPSH also stay almost the same places as in the 20Cs, only are stronger.

The same analysis as before is applied, including WPSH in the future as a covariate into the PP model (Figure 4.7). Non-stationary models instead of the stationary model have been selected as the best model in most parts of mid- and southern China including Tibet, which implies a strong influence of WPSH on extreme rainfall. The overall slope of the location parameter in model 1 is positive in these regions, suggesting a positive influence of WPSH on extreme rainfall. Negative influence of WPSH index can be found in some grid points in northern China.

20C1:

20C2:

20C3:
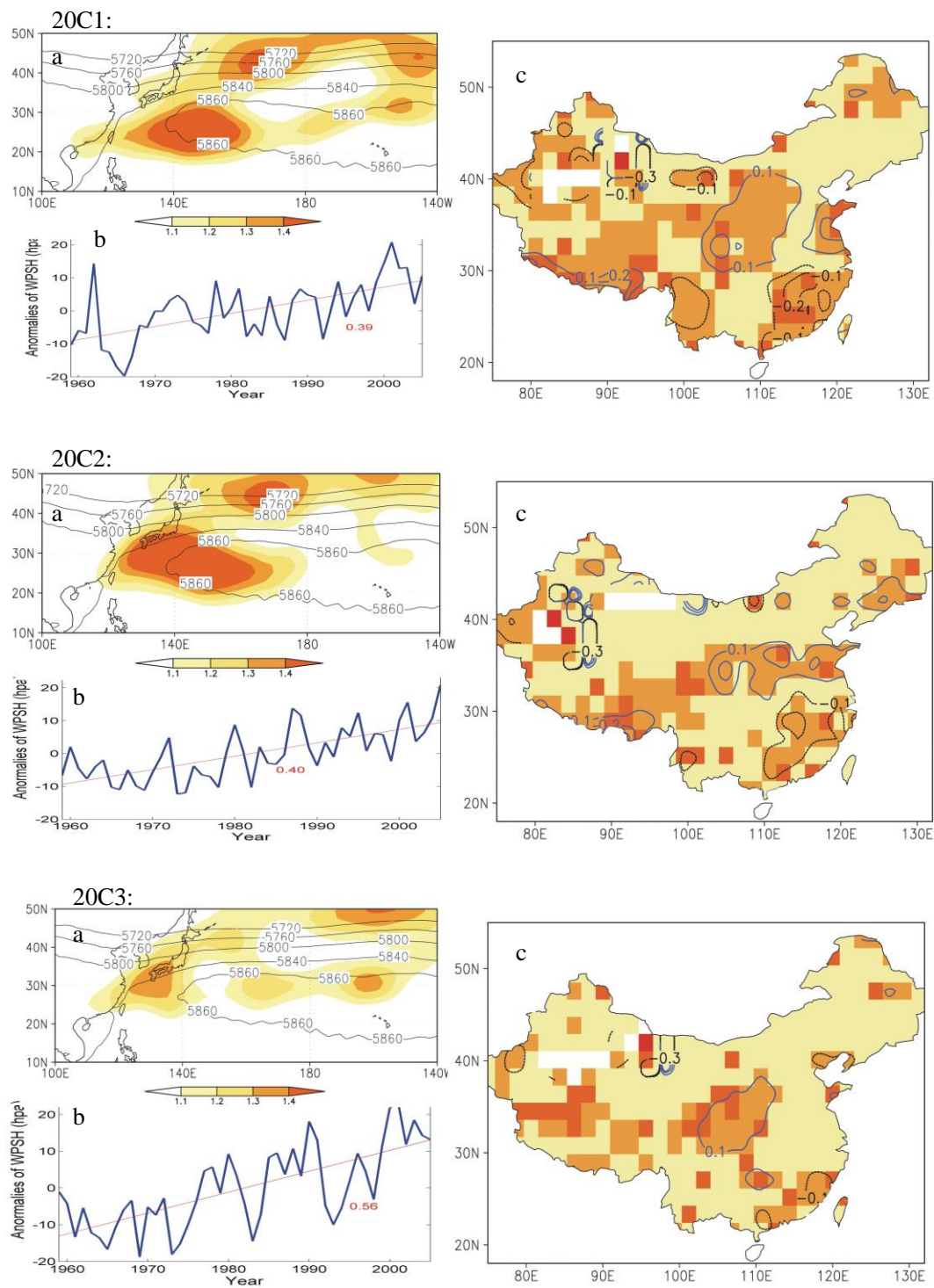
Figure 4.6: (a) Same as figure 4.3a (b) Time series of WPSH anomalies and its linear trend (c) Same as figure 4.2b but for 20C ensemble runs using WPSH as a covariate.
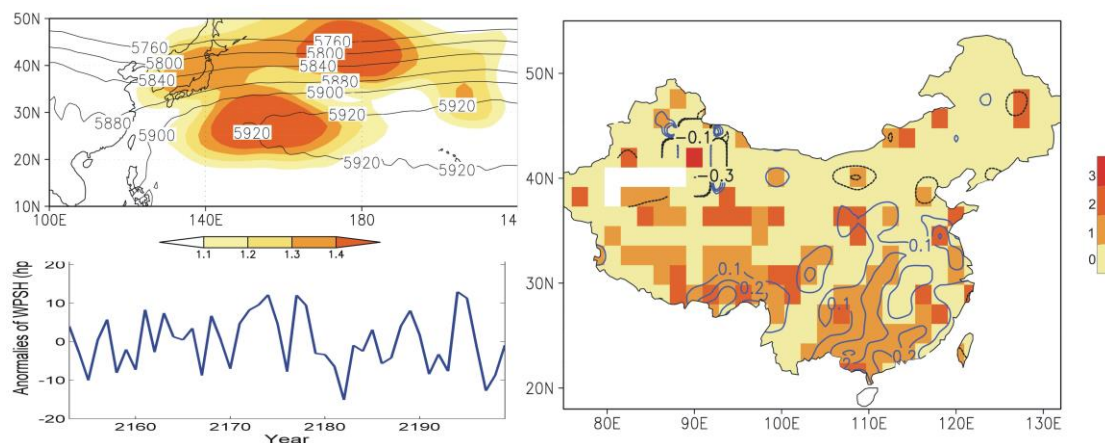
Figure 4.7: The same as figure 4.6 but for RCP4.5 run.

GCMs simulated climate change of the distribution of extreme rainfall events (stationary model):

The same analysis is applied to the future extreme rainfall events for the period of 2153–2199 under RCP4.5. The PP model parameters and RV20 in future climatology and their significant changes (10% significance level) are illustrated and compared with the 20C ensemble mean in Figure 4.8. The changes in the location parameters and RV20 (Figure 4.8a, d, right) are generally significant in China: increase for most parts but a decrease for the southern Tibetan Plateau and the central part of northeastern and northern China. Increasing RV20 also suggests a decrease in the return period of a certain extreme rainfall event. The scale parameter (Figure 4.8b, right) is similar to the changes of the location and RV20, an increase in mid southern China and decrease in southern Tibet. The shape parameter (Figure 4.8c, left) for most parts with the exception of some parts in northeastern China stays negative which implies that extreme rainfall remains Weibull distributed. Compared with 20C only a few scattering stations in northern China change.
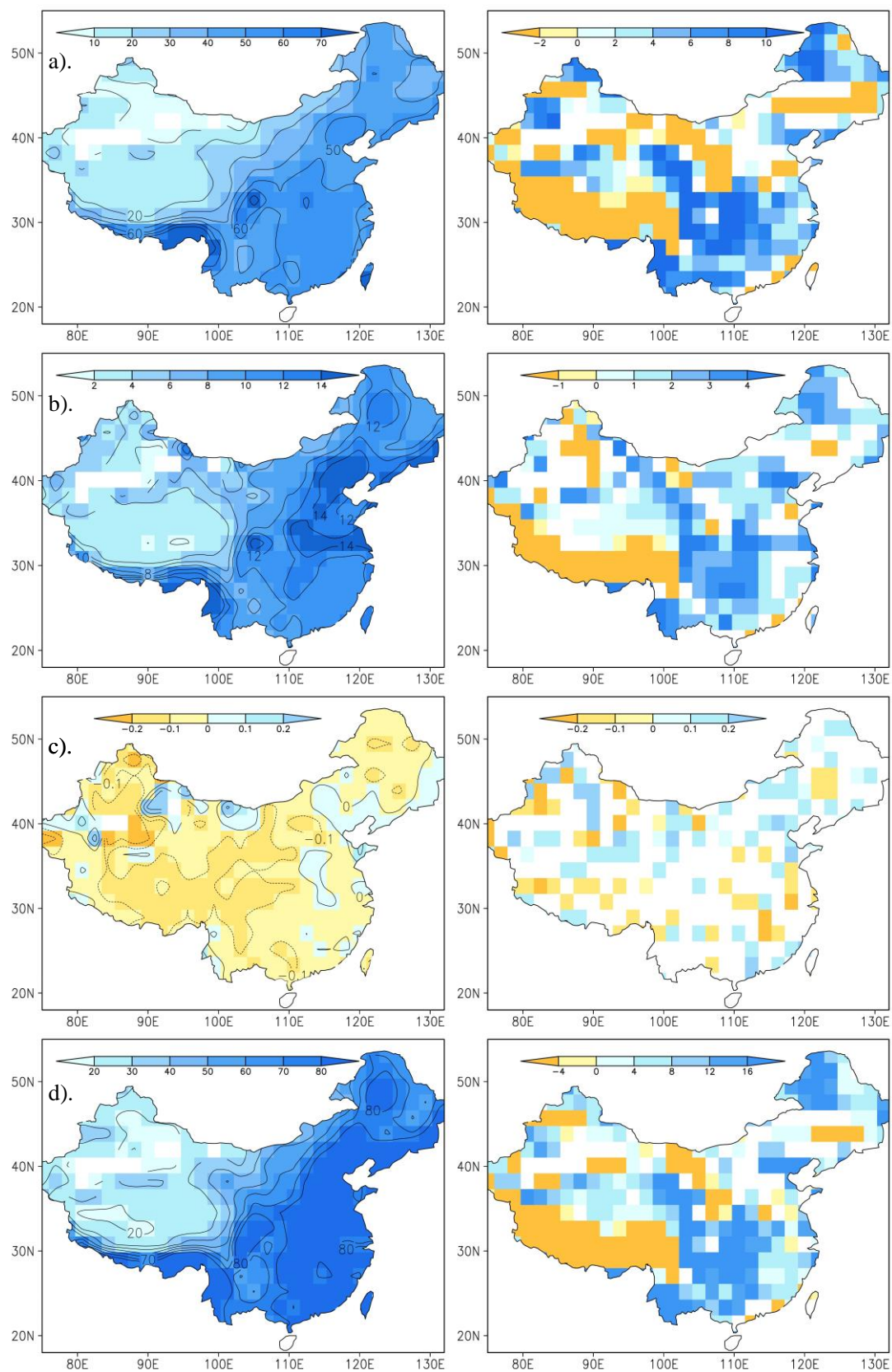
Figure 4.8: Left column: same as figure 4.1 but for RCP4.5 run; Right column: significant difference of the PP parameters (a, location; b, scale; c, shape) and (d) RV20 between the RCP4.5 (2153–2199) and 20C1 (1959–2005) run.

4.5 Summary

In this study, the Point Process (PP) model is employed to fit daily extreme rainfall events in warm season over China. It shows abilities to represent the correct spatial pattern of extreme rainfall events. The non-stationary PP model is applied to estimate trends of extreme events, and then reveal almost no significant trends in general. Furthermore, PP is employed to build a relationship between Western Pacific Subtropical High, which is one of the most important large-scale atmospheric circulation systems affecting the East Asia summer monsoon, and its local extreme rainfall. Results show the WPSH significantly influence extreme rainfall in most area except south China. Based on the relationship using calibration data in the period 1959–2005, the projection of WPSH anomalies can be used to predict the changes of extreme rainfall. A comparison between projected changes using the statistical non-stationary model and the observed one, in two periods 1959–1979 and 1980–2000, is given and shows a good matching. Overall, with higher WPSH, extreme rainfall has less risk in the north China, and higher risk in southern China and the north border of northeastern China.

A comparison of the 20C ensemble simulations with the observation for the time period between 1959 and 2005 showed that the MPI-ESM overall simulated the pattern of the rainfall extremes expressed by the parameters and the 20-year return value of the stationary PP well, but the intensity is underestimated because the GCMs simulated extremes normally represent a grid-point mean of extremes. However, the simulated rainfall extremes in China are Weibull distributed, while the observed ones are Frechet distributed in general.

The differences in distribution parameters and RV20 estimated by the stationary PP model between the 20C and RCP4.5 simulations were assessed. Results show significant changes of the mean (location parameter), variance (scale parameter) and 20-year return value in almost the whole China in future scenario RCP4.5: increase in southern China and the northern part of northeastern China, and decrease in Tibet and central- northeastern China.

Chapter 5

Summary and Outlook

5.1 Summary and conclusion

The well-known Jennings law of observed extreme rainfall events versus their duration, which covers a wide range of spatial and temporal scales is revisited using Global Climate Model (GCM) simulations (Chapter 2) and is conceptually interpreted by truncating a first order autoregressive model (Chapter 3). Extreme value distributions of daily time scales are used to relate extreme rainfall statistics to large-scale circulation dynamics. This point process model, which is tested for the warm season in China related to the Summer Monsoon system characterized by the Western Pacific Subtropical High (WPSH), can be considered as a first step towards downscaling extreme value statistics. Overall, the study answered the following questions:

Can GCMs simulations with different resolutions (T63 and T31) reproduce Jennings scaling law, that is the observed maximum rainfall-duration scaling-law relationship?
Can Jennings scaling law be found in single grid-points?
What kind of information is embedded in the scaling exponent?
Do extremes in a warmer climate increase simultaneously on all different time scales compared to the present-day climate?

Yes, the Jennings scaling law, $P \sim d^{\,b}$ has been substantiated for three decades of the scaling regime using simulations of spectral and gridpoint GCMs, where the analysis is confined to daily rainfall records. The maximum rainfall-duration scaling-law exponents are $b \approx 0.5$ in the higher resolutions (EH5OM T63L31, EH6OM and HadGEM) compared to $b \approx 0.7$ for the lower resolution GCM EH5OM (T31L19).

Yes, the similar scaling phenomena are found at few grid points which generate few extreme spells contributing the global records.

Based on the generalized structure function, the scaling exponent was found to be equal to the Hurst exponent. The increase of the scaling exponent from 0.5 to 0.7 (with increasing resolution) may indicate a random process modified by enhanced

persistence (Zhu et al., 2010).

In the warmer climate (RCP8.5) the intensity in the maximum rainfall events increases by about 50% for durations of days, but vanishes for monthly time scales.

Can we construct a simple model to simulate Jennings' scaling law? What is the mechanism explanation?

Yes. A truncated (censored) AR(1) is introduced to explain the scaling behavior oft he single station maximum rainfall depth-duration for two orders of magnitude. The dynamics behind the underlying AR(1) is introduced as a surrogate model for atmospheric water fluxes. By implementing the censorship the downward fluxes are truncated and only the positive (upward) fluxes are kept. Thus intermittency is introduced, which leads to the nonlinear scaling behavior documented by Jennings law.

How to relate daily-scale extreme rainfall events with large-scale circulation to understand the dynamics of generation of extremes?

Non-stationary PP models are employed to build a relationship between daily extreme rainfall events over China and Western Pacific Subtropical High (WPSH), which is one of the most influential East Asia summer monsoon systems. The results show that a high phase of WPSH which indicates that the subtropical high extending more westward and with stronger intensity, corresponds to a substantially increased likelihood of extreme rainfall over North China, but a decreased likelihood of extreme rainfall over southern China and the northern border of northeastern China.

5.2 Future research

As shown in Chapter 4, the MPI-ESM is able to represent observed patterns of large-scale rainfall extremes over eastern China. However, simulations in some regions can be improved, for example, the southern and eastern edges of Tibet with its complex orography. Moreover, the relation between WPSH and extreme rainfall is incorrectly represented over southeast China, and possibly due to the absence of meso-scale systems (e.g. typhoon) in T63 simulations. These problems could be improved by increasing the horizontal resolution of CGCMs.

Large-scale atmospheric circulation patterns are important for the understanding and interpretation of changes of extreme climate events. The inclusion of WPSH in the statistical modeling of warm season extreme rainfall statistics can explain most of the variability of the extreme rainfall over China. In former studies, 500-hpa geopot-

ential height is commonly used as a predictor for summer rainfall in the context of statistical downscaling (Zhu et al., 2008; Wei and Huang, 2010). However, the relationship between WPSH and extreme rainfall over China in simulations is overall underestimated. The reason might be the location of WPSH which, shifting eastward, also leads to rainfall systems centered further eastward.

The statistical modeling of extreme value distributions can be further expanded and improved introducing other potential predictor candidates: high time resolution water vapor (based on GPS-systems, see Bordi et al 2013), land-ocean sea level pressure or temperature differences, 850-hPa zonal and meridional velocity and 200-hPa zonal velocity, or circulation regimes.

Bibliography

Akaike, H., 1974: A new look at the statistical model identification. *IEEE Trans. Automat. Contl.,* **19**, 716–723.

Alexander, L. V., X. Zhang, and co-authors, 2006: Global observed changes in daily climate extremes of temperature and precipitation. *J. Geophys. Res.,* **111**, D05109.

Alexander, L. V., and J. M. Arblaster, 2009: Assessing trends in observed and modelled climate extremes over Australia in relation to future projections. *International Journal of Climatology,* **29**: 417 – 435.

Austin, P. M., and R. A. Houze, 1972: Analysis of the Structure of Precipitation Patterns in New England. *J. Appl. Meteor.,* **11**, 926–935.

Bachner, S., A. Kapala, and C. Simmer, 2008: Evaluation of daily precipitation characteristics in the CLM and their sensitivity to parameterizations. *Meteorologische Zeitschrift*, **17(4)**, 407–420.

Bates, B. C., Z. W. Kundzewicz, S. Wu, and J. P. Palutikof, 2008: *Climate Change and Water*. Technical Paper of the Intergovernmental Panel on Climate Change. Geneva, IPCC Secretariat.

Bell, J. L., L. C. Sloan, and M. A. Snyder, 2004: Regional Changes in Extreme Climatic Events: A Future Climate Scenario. *J. Climate*, **17**, 81–87.

Benestad, R. E., 2006: Can we expect more extreme precipitation on the monthly time scale? *J. Clim.,* **19**, 630–637.

Beniston, M., and D. Stephenson, 2004: Extreme climatic events and their evolution under changing climatic conditions. *Glob Planet Change,* **44**, 1–9

Blender, R., X. Zhu, and K. Fraedrich, 2011: Observation and modelling of 1/f-noise in weather and climate. *Advances in Science and Research*, **6**, 137–140.

Bordi, I., K. Fraedrich, A. Sutera, and X. Zhu, 2013: Ground-based GPS measurements: Time behavior from half-hour to years. *Theor. Appl. Climatol.,* doi: 10.1007/s00704-013-0923-z.

Caskey, J. E., 1963: A Markov Chain for the probability of precipitation occurrence in intervals of various lengths. *Mon. Weath. Rev.*, **91**, 298–301.

Bibliography

Chen, C. T., and T. Knutson, 2008: On the verification and comparison of extreme rainfall indices from climate models. *Journal of Climate*, **21(7)**, 1605–1621.

Christensen, J. H., F. Boberg, O. B. Christensen, and P. Lucas-Picher, 2008: On the need for bias correction of regional climate change projections of temperature and precipitation. *Geophysical Research Letters*, **35(20)**, L20709.

Cohen, A. J., 1959: Simplified estimators for the normal distribution when samples are singly censored or truncated. *Technometrics,* **1**, 217–237.

Coles, S., 2001: *An Introduction to Statistical Modeling of extreme values*. Springer Verlag, London, UK., 205pp.

Coles, S., and L. Pericchi, 2003: Anticipating catastrophes through extreme value modelling. *Appl. Stat.*, **53**, 405–416.

Crane, R. K., 1990: Space-time structure of rain rate fields. *J. Geophys. Res.*, **95**, 2001– 2020.

Curriero, F. C., J. A. Patz, J. B. Rose, and S. Lele, 2001: The association between extreme precipitation and waterborne disease outbreaks in the United States, 1948–1994. *American Journal of Public Health*, **91(8)**, 1194–1199.

Davis, A., A. Marshak, W. Wiscombe, and R. Cahalan, 1994: Multifractal characterizations of nonstationarity and intermittency in geophysical fields: Observed, retrieved, or simulated. *J. Geophys. Res.*, **99**, 8055–8072.

Dhar, O. N., and S. M. T. Farooqui, 1973: A Study of rainfalls recorded at the Cherrapunji Observatory. *Hydrological Sciences Bulletin,* **18(4),** 441–450.

Doswell, C. A. III, H. E. Brooks, and R. A. Maddox, 1996: Flash flood forecasting: An ingredients-based methodology. *Wea. Forecasting*, **11**, 560–581.

Durman, C. F., J. M. Gregory, D. C. Hassell, R. G. Jones, J. M. Murphy, 2001: A comparison of extreme European daily precipitation simulated by a global and a regional climate model for present and future climates. *Quarterly Journal of the Royal Meteorological Society*, **127**: 1005 – 1015.

Eagleson, P. S., 1970: *Dynamic Hydrology*, pp. 200, figure 11–25, McGraw-Hill, New York, N.Y.

Easterling, D. R., G. A. Meehl, C. Parmesan, S. A. Changnon, T. R. Karl, L. O. Mearns, 2000: Climate extremes: observations, modeling, and impacts. *Science* **289**: 2068–2074.

Feder, J., 1988: *Fractals*. New York: Plenum Press.

Feng, S., S. Nadarajah, and Q. Hu, 2007: Modeling annual extreme precipitation in China using the generalized extreme value distribution. *Journal of Meteorological Society of Japan*, **85 (5)**, 599‑613

Feser, F., B. Rockel, H. von Storch, J. Winterfeldt, and M. Zahn, 2011: Regional Climate Models Add Value to Global Model Data: A Review and Selected Examples. *Bull. Amer. Meteor. Soc.*, **92**, 1181–1192.

Feyerherm, A. M., and L.D. Bark, 1965: Statistical methods for persistent precipitation pattern. *J. Appl. Meteorol.*, **4**, 320–328.

Feyerherm, A. M. and L. D. Bark, 1967: Goodness of fit of Markov chain model for sequences of wet and dry days. *J. Appl. Meteorol.*, **6**, 770–773.

Fisher, R. A., and L. H. C. Tippett, 1928: Limiting forms of the frequency distribution of the largest and smallest member of a sample, *Proc. Camb. Phil. Soc.*, **24**, 180–190.

Foley, A. M., 2010: Uncertainty in regional climate modelling: A review. *Prog. Phys. Geogr.*, **34**, 647–670,

Fraedrich, K., and C. Larnder, 1993: Scaling regimes of composite rainfall time series. *Tellus*, **45A,** 289–298.

Fraedrich, K., and C. Ziehmann, 1994: Predictability experiments with persistence forecasts in a red-noise atmosphere. *Q. J. R. Meteorol. Soc.,* **120**, 387–428.

Fraedrich, K., R. Blender, and X. Zhu, 2009: Continuum climate variability: long-term memory, scaling, and 1/f –noise. *Int. J. Mod. Phys.,* **B23,** 5403–5416.

Gabriel, K. R. and J. Neumann, 1962: A Markov chain model for daily rainfall occurrences in Tel Aviv. *Israel. J. Roy. Meteorol. Soc.*, **88**, 90–95.

Galmarini, S., D. G. Steyn, and B. Ainslie, 2004: The scaling law relating world point-precipitation records to duration, *Int. J. Climatology*, **24(5)**, 533–546.

Giorgi, F., and L. O. Mearns, 1999: Introduction to special section: regional climate modeling revisited. *Journal of Geophysical Research,* **104**, 6335–6352.

Groisman, P. Y., R. W. Knight, D. R. Easterling, T. R. Karl, G. C. Hegerl, and V. N. Razuvaev, 2005: Trends in Intense Precipitation in the Climate Record. *J. Climate*, **18**, 1326–1350.

Bibliography

Gutenberg, B., and C. F. Richter, 1954: *Seismicity of the Earth and Associated Phenomena*, Princeton Univ. Press, Princeton, N. J. 310pp.

Haerter, J. O., S. Hagemann, C. Moseley, and C. Piani, 2011: Climate model bias correction and the role of timescales, *Hydrology and Earth System Sciences*, **15**, 1065–1079.

Hannachi, A., 2012: Intermittency, autoregression and censoring: a first-order AR model for daily precipitation. *Meteorol Applications*, doi: 10.1002/met.1353.

Harris, D., E. Foufoula-Georgiou, K. K. Droegemeier, and J. J. Levit, 2001: Multiscale statistical properties of a high-resolution precipitation forecast, *J. Hydrometeor.,* **2**, 406 – 418.

Holman, K. D., and S. J. Vavrus, 2012: Understanding Simulated Extreme Precipitation Events in Madison, Wisconsin, and the Role of Moisture Flux Convergence during the Late Twentieth and Twenty-First Centuries. *J. Hydrometeor.*, **3**, 877–894.

Hu, Z.Z., S. Yang, and R. Wu, 2003: Long-term climate variations in China and global warming signals. *J. Geophys. Res.*, **108**, 4614.

Hubert, P., Y. Tessier, S. Lovejoy, D. Schertzer, F. Schmitt, P. Ladoy, J. P. Carbonnel, and S. Violette, 1993: Multifractals and extreme rainfall events. *Geophysical Research Letters,* **20(10)**, 931–934.

Hurst, H. E., 1951: Long-term storage capacity of reservoirs. *Transactions of the American Society of Civil Engineers*, **116**, 770–799.

Hurvich, C. M., and C-L. Tsai, 1989: Regression and time series model selection in small samples. *Biometrika,* **76**, 297–307.

IPCC Climate Change 2007: *The Physical Science Basis* (eds Solomon, S. et al.), Cambridge University Press

IPCC Climate Change 2012: *Summary for policymakers. Intergovernmental Panel on Climate Change Special Report on Managing the Risks of Extreme Events and Disasters to Advance Climate Change Adaptation*, (eds CB Field et al.), Cambridge University Press, pp1–19

Jennings, A. H., 1950: World's greatest observed point rainfalls. *Mon. Wea. Rev.,* **78(1)**, 4–5.

Jimoh, O. D., and P. Webster, 1996: Optimum order of Markov chain for daily rainfall in Nigeria. *J. Hydrol.*, **185**, 45–69.

Jimoh, O. D. and P. Webster, 1999: Stochastic modelling daily rainfall in Nigeria, intra-annual variation of model parameters. *J. Hydrol.*, **222**, 1–17.

Jones, C. D., and Coauthors, 2011: The HadGEM2-ES implementation of CMIP5 centennial simulations. *Geosci. Model Dev.*, **4**, 543–570.

Jones, P., C. Harpham, C. Kilsby, V. Glenis, and A. Burton, 2009: Projections of future daily climate for the UK from the Weather Generator. UK, UK Met Office.

Kalnay, E., and Coauthors, 1996: The NCEP/NCAR 40-Year Reanalysis Project. *Bull. Amer. Meteor. Soc.*, **77**, 437–471.

Karl, T. R., and R. W. Knight, 1998: Secular Trends of Precipitation Amount, Frequency, and Intensity in the United States. *Bull. Amer. Meteor. Soc.*, **79**, 231–241.

Kattsov, V. M., J. E. Walsh, W. L. Chapman, V. A. Govorkova, T. V. Pavlova, and X. Zhang, 2007: Simulation and projection of Arctic freshwater budget components by the IPCC AR4 Global Climate Models. *J. Hydrometeor.*, **8**, 571– 589.

Katz, R. W., 1999: Extreme value theory for precipitation: Sensitivity analysis for climate change. *Adv. Water Resour.*, **23**, 133–139.

Katz, R. W., G. S. Brush, and M. B. Parlange, 2005: Statistics of extremes: Modeling ecological disturbance. *Ecology*, **86(5)**, 1124–1134.

Katz, R., M. Parlange, and P. Naveau, 2002: Statistics of extremes in hydrology. *Advances in Water Resources,* **25**, 1287–1304.

Kelman, J., 1977: *Stochastic modeling of hydrologic intermittent daily process.* Hydrology paper **89**. Colorado State University: Fort Collins, CO.

Kharin, V. V., and F. W. Zwiers, 2000: Changes in the extremes in an ensemble of transient climate simulations with a coupled atmosphere-ocean GCM. *Journal of Climate*, **13**, 3760–3788.

Kharin, V. V., and F. W. Zwiers, 2005: Estimating extremes in transient climate change simulations. *J. Climate*, **18**, 1156–1173.

Bibliography

Kharin, V. V., F. W. Zwiers, X. Zhang, and G. C. Hegerl, 2007: Changes in temperature and precipitation extremes in the IPCC ensemble of global coupled model simulations, *J. Climate*, **20**, 1419–1444.

Kharin, V. V., F. Zwiers, X. Zhang, and M. Wehner, 2013: Changes in temperature and precipitation extremes in the CMIP5 ensemble. *Climatic Change*, **119 (2)**, 345–357.

Kistler, R., and Coauthors, 2001: The NCEP–NCAR 50–Year Reanalysis: Monthly Means CD–ROM and Documentation. *Bull. Amer. Meteor. Soc.*, **82**, 247–267.

Klein Tank, A., F. Zwiers, and X. Zhang, 2009: *Guidelines on analysis of extreme in a changing climate in support of informed decisions for adaptation*. Geneva, Switzerland, WMO. Report number: WCDMP-No. 72.

Kunkel, K. E., K. Andsager, and D. R. Easterling, 1999: Long-Term Trends in Extreme Precipitation Events over the Conterminous United States and Canada. *J. Climate*, **12**, 2515–2527.

Lenderink, G., and E. Van Meijgaard, 2008: Increase in hourly precipitation extremes beyond expectations from temperature changes. *Nature Geoscience*, **1(8)**, 511–514.

Li, Y., W. Cai, and E. P. Campbell, 2005: Statistical modeling of extreme rainfall in southwest Western Australia. *J. Climate*, **18**, 852–863.

Lovejoy, S., and B. Mandelbrot, 1985: Fractal properties of rain, and a fractal model. *Tellus*, Ser. **A**, **37**, 209–232.

Lovejoy, S., and D. Schertzer, 1985: Generalized scale invariance in the atmosphere and fractal models of rain. *Water Resour. Res.*, **21**, 1233–1250.

Lovejoy, S., and D. Schertzer, 1990: Fractals, raindrops and resolution dependence of rain measurements. *J. Appl. Meteorol.,* **29(11)**, 1167–1170

Lovejoy, S., and D. Schertzer, 2006: Multifractals, cloud radiances and rain. *J. Hydrol.,* **322(1-4)**, 59–88

Lowry, W. P., and D. Guthrie, 1968: Markov chains of order greater than one. *Mon. Weath. Rev.*, **96**, 798–801.

Lu, R., 2002: Indices of the summertime western North Pacific subtropical high. *Adv. Atmos. Sci.*, **19(6)**, 1004–1028

Mandelbrot, B. B., 1983: *The Fractal Geometry of Nature*. New York: W.H. Freeman & Company.

Mandelbrot, B. B., and Wallis J. R., 1969: Some long-run properties of geophysical records. *Water Resources Research*: **5(2)**, 321–340.

Maraun, D., F. Wetterhall, and co-authors, 2010: Precipitation downscaling under climate change: Recent developments to bridge the gap between dynamical models and the end user. *Reviews of Geophysics*, **48(3)**, RG3003

Marani, M., 2003: On the correlation structure of continuous and discrete point rainfall. *Water Resour. Res.*, **39(5)**, 1128.

Marani, M., 2005: Non-power-law-scale properties of rainfall in space and time. *Water Resour. Res.*, **41**, W08413.

Min, S., X. Zhang, F. W. Zwiers, and G. C. Hegerl, 2011: Human contribution to more-intense precipitation extremes. *Nature,* **470**, 378–381.

Murphy, J., 2000: Predictions of climate change over Europe using statistical and dynamical downscaling methods. *International Journal of Climatology*, **20**, 489–501.

National Weather Service, 2013: *World record point precipitation measurements*. http://www.nws.noaa.gov/oh/hdsc/record_precip/record_precip_world.html

NCC (National Climate Center), 1998: *China's 1998 Severe Flood and Climate Extremes*. China Meteorological Press, 137 pp (in Chinese)

Paulhus, J. L. H., 1965: Indian Ocean and Taiwan rainfalls set new records, *Mon. Wea. Rev.,* **93(5)**, 331–335.

Rauscher, S. A., E. Coppola, C. Piani, and F. Giorgi, 2009: Resolution effects on regional climate model simulations of seasonal precipitation over Europe. *Climate Dynamics*, 1–27.

Richardson, C. W., 1981: Stochastic simulation of daily precipitation, temperature and solar radiation. *Water Resour. Res.*, **17**, 182–190.

Roeckner, E., and Coauthors, 2006: Sensitivity of Simulated Climate to Horizontal and Vertical Resolution in the ECHAM5 Atmosphere Model, *J. Climate*, **19**, 3771–3791.

Bibliography

Rosenzweig, C., F. N. Tubiello, R. A. Goldberg, E. Mills, and J. Bloomfield, 2002: Increased crop damage in the US from excess precipitation under climate change. *Global Environ Change,* **12**, 197–202.

Rummukainen, M., 2010: State-of-the-art with regional climate models. *WIREs Climate Change*, **1**, 82–96.

Schertzer, D., and S. Lovejoy, 1987: Physical modeling and analysis of rain and clouds by anisotropic scaling multiplicative processes. *J. Geophys. Res.,* **92**, 9693–9714

Schmidhuber, J., and F. N. Tubiello, 2007: Global food security under climate change. *Proceedings of the National Academy of Sciences*, USA 104, 19703–19708.

Selvalingam, S. and M. Miura, 1978: Stochastic modelling of monthly and daily rainfall sequences. *Water Resour. Bull.*, **14**, 1105–1120.

Sillmann, J., M. Kallache, M. Croci-Maspoli, and R.W. Katz, 2011: Extreme cold winter temperatures in Europe under the influence of North Atlantic atmospheric blocking. *Journal of Climate*, **24**, 5899–5913

Srikanthan, R., and T. A. McMahon, 2001: Stochastic generation of annual, monthly and daily climate data: A review. *Hydrology and Earth System Sciences,* **5(4)**, 653–670

Stephens, M. A., 1970: Use of Kolmogorov-Smirnov, Cramer-von-Mises and related statistics without extensive tables. *Journal of the Royal Statistical Society*, **32B**, 115–122.

Stephens, G. L., J. Li, and co-authors, 2012: An update on Earth's energy balance in light of the latest global observations. *Nature Geoscience*, **5**, 691–696.

Stern, R. D., 1980: Computing probability distribution for the start of the rains from a Markov chain model for precipitation. *J. Appl. Meteorol.*, **21**, 420–423.

Stern, R. D., and R. Coe, 1984: A model fitting analysis of daily rainfall data. *J. Roy. Statist. Soc. A*, **147**, Part 1, 1–34.

Stevens, B., and co-authors, 2013: Atmospheric component of the MPI-M Earth System Model: ECHAM6, *J. Adv. Model. Earth Syst.*, **5(2)**, 146–172

Solanki, A., 2013, "India raises flood death toll reaches 5,700 as all missing persons now presumed dead", *CBSNEWS*, Retrieved June 16 http://www.cbsnews.com/8301-202_162-57593939/india-raises-flood-death-toll-reaches-5700-as-all-missing-persons-now-presumed-dead/

Sui, C., P. Chung, and T. Li, 2007: Interannual and interdecadal variability of the summertime western North Pacific subtropical high. *Geophys. Res. Lett.*, **34**, L11701, doi:10.1029/2006GL02920

Tebaldi, C., K. Hayhoe, J. M. Arblaster, and G. A., Meehl, 2006: Going to the extremes: an intercomparison of model-simulated historical and future changes in extreme events. *Clim. Change*, **79**, 185–211.

Tessier, Y., S. Lovejoy, and D. Schertzer, 1993: Universal multifractals: Theory and observations for rain and clouds, *J. Appl. Meteorol.*, **32**, 223–250.

Tessier, Y., S. Lovejoy, P. Hubert, D. Schertzer, and S. Pecknold, 1996: Multifractal analysis and modeling of rainfall and river flows and scaling, causal transfer functions. *J. Geophy. Res. Atmos.,* **101**(D21), 26427–26440

Trenberth, K. E., 2011: Changes in precipitation with climate change. *Clim. Res.,* **47**, 123–138

Trenberth, K. E., and J. Hurrell, 1994: Decadal atmosphere–ocean variations in the Pacific. *Climate Dyn.*, **9**, 303–319.

Uppala, S. M., and Coauthors, 2005: The ERA-40 reanalysi*s*. Q. J. R. Meteorol. Soc., **131**, 2961–3012

Veneziano, D., A. Langousis, and P. Furcolo, 2006: Multifractality and rainfall extremes: A review, *Water Resour. Res.*, **42**, W06D15.

Verrier, S., L. de Montera, L. Barthès, and C. Mallet, 2010: Multifractal analysis of African monsoon rain fields, taking into account the zero rain-rate problem. *J. Hydrol.,* **389(1–2)**, 111–120

von Storch, H., H. Langenberg, and F. Feser, 2000: A spectral nudging technique for dynamical downscaling purposes. *Monthly Weather Review*, **128(10),** 3664–3673.

Wang, B., B. Xiang, and J-Y. Lee, 2013: Subtropical High predictability establishes a promising way for monsoon and tropical storm predictions. *PNAS*, doi:10.1073/pnas.1214626110.

Bibliography

Wang, J., and X. Zhang, 2008: Downscaling and projection of winter extreme daily precipitation over North America, *J. Clim.*, **21(5)**, 923–937.

Wang, S., and E. Yu, 2013: Simulation and projection of changes in rainy season precipitation over China using the WRF model. *Acta. Meteor. Sinica.*, **27(4)**, 577–584.

Wei, F. and J. Huang, 2010: A study of predictability for summer precipitation on East China using downscaling techniques. *J. Trop. Meteor.*, **26**, 483–488

Weiss, L. L., 1964: Sequences of wet and dry days described by a Markov chain model. *Mon. Weath. Rev.*, **92**, 169–176.

Wieczorek, G. F., and P. P. Leahy, 2008: Landslide hazard mitigation in North America, Environ. *Eng. Geosci.*, **14**, 133–144.

Wilby, R. L., S. P. Charles, E. Zorita, B. Timbal, P. Whetton, and L. O. Mearns, 2004: Guidelines for use of climate scenarios developed from statistical downscaling methods. *IPCC Data Distribution Centre Report*, UEA, Norwich, UK, 27.

World Meteorological Organization, 1986: *Manual for Estimation of Probable Maximum Precipitation*, 2nd ed. Operational Hydrology Report Number 1, WMO Number 332, WMO: Geneva, Switzerland.

World Meteorological Organization, 1995: *Guide to Hydrological Practices*, 5th ed. WMO No. 168, WMO: Geneva, Switzerland.

Wu, B., and T. Zhou, 2008: Oceanic origin of the interannual and interdecadal variability of the summertime western Pacific subtropical high. *Geophysical Research Letters*, **35**, L13701, doi:10.1029/2008GL034584

Yang, H., and S. Sun, 2003: Longitudinal displacement of the subtropical high in the western Pacific in summer and its influence. *Adv. Atmos. Sci.*, **20**, 921–933

Yang, H., and S. Sun, 2005: The characteristics of longitudinal movement of the subtropical high in the western Pacific in pre-rainy season in South China. *Adv. Atmos. Sci.*, **22**, 392–400

Yano, J. I., R. Blender, C. Zhang, and K. Fraedrich, 2004: 1/f - Noise and pulse-like events in the tropical atmospheric surface variabilities. *Q. J. R. Meterol. Soc.*, **130**, 1697–1721.

You, Q. L. and co-authors, 2011: Changes in daily climate extremes in China and their connection to the large scale atmospheric circulation during 1961–2003. *Climate Dynamics*, **36(11-12)**, 2399–2417

Yu, R., and T. Zhou, 2007: Seasonality and three-dimensional structure of interdecadal change in the East Asian monsoon. *J. Climate*, **20**, 5344–5355.

Zawadzki, I. I., 1973: Statistical properties of precipitation patterns, *J. Appl. Meteorol.*, **12**, 459–472.

Zhai, P., and F. Ren, 1999: On change of China's maximum and minimum temperatures in 1951–1990. *Acta Meteor. Sin.*, **13** (2), 278–290.

Zhai, P., A. Sun, F. Ren, X. Liu, B. Gao, and Q. Zhang, 1999: Changes of climate extremes in China. *Climate Change*, **42**, 203–218

Zhai, P., X. Zhang, H. Wan, and X. Pan, 2005: Trends in total precipitation and frequency of daily precipitation extremes over China. *J. Climate*, **18**, 1096–1108

Zhang, H., K. Fraedrich, R. Blender, and X. Zhu, 2013: Precipitation extremes in CMIP5 simulations on different time scales. *J. Hydrometeor,* **14**, 923–928

Zhang, X., 2013, "Storms across nation cause landslides, collapse bridges", *Global Times*. July 10, Retrieved from
http://www.globaltimes.cn/content/795342.shtml#.Ui7EOn_U8_k

Zhu, C., C. Park, W. Lee, and W. Yun, 2008: Statistical downscaling for multi-model ensemble prediction of summer monsoon rainfall in the Asia-Pacific region using geopotential height field. *Adv. Atmos. Sci.*, **25**, 867–884

Zhu, X., K. Fraedrich, Z. Liu, and R. Blender, 2010: A demonstration of long term memory and climate predictability. *J. Climate*, **23**, 5021–5029.

Bibliography

List of Publications

Published or accepted Papers

Zhang, H., K. Fraedrich, R. Blender, and X. Zhu, 2013: Precipitation extremes in CMIP5 simulations on different time scales. *J. Hydromet*., 14, 923-928. doi: 10.1175/JHM-D-12-0181.1.

Zhang, H., K. Fraedrich, X. Zhu, and R. Blender, 2013: World's greatest observed point rainfalls: Jennings (1950) scaling law. *J. Hydromet.,* 14, in press. doi: 10.1175/JHM-D-13-074.1

Unpublished Working Paper

Zhang, H., F. Sienz, X. Zhu, K. Fraedrich and R. Blender, Influence of Western Pacific Subtropical High on extreme daily precipitation in warm season over China, in preparation

List of Publications

Acknowledgements

Eidesstattliche Versicherung *Declaration on oath*

Hiermit erkläre ich an Eides statt, dass ich die vorliegende Dissertationsschrift selbst verfasst und keine anderen als die angegebenen Quellen und Hilfsmittel benutzt habe.

I hereby declare, on oath, that I have written the present dissertation by my own and have not used other than the acknowledged resources and aids.

Hamburg, den   Unterschrift
Hamburg, date   Signature